geosciences

MDPI

Article

Structural Control and Timing of the Iron-Oxide-Copper-Gold (IOCG) Skarn Formation at Tatatila-Las Minas Mining District (Central Mexico)

Martina Zucchi [1,*], Emmanuel Olvera-García [2], Domenico Liotta [1], Andrea Brogi [1,3,4], Alfredo Caggianelli [1], Marinella Ada Laurenzi [5], Walter H. Wheeler [6], Caterina Bianco [1], Fidel Gómez-Alvarez [2], Sergio Najera-Blas [7], Adrián Jiménez-Haro [8], Jorge Alejandro Guevara-Alday [9], Guia Morelli [10], Gennaro Ventruti [1], Andrea Orlando [10] and Giovanni Ruggieri [10]

1 Department of Earth and Geoenvironmental Sciences, University of Bari, 70125 Bari, Italy; domenico.liotta@uniba.it (D.L.); andrea.brogi@uniba.it (A.B.); alfredo.caggianelli@uniba.it (A.C.); caterina.bianco@regione.puglia.it (C.B.); gennaro.ventruti@uniba.it (G.V.)
2 Instituto de Investigaciones en Ciencias de la Tierra, Universidad Michoacana de San Nicolás de Hidalgo, Morelia 58030, Mexico; emmanuel.olvera.garcia@umich.mx (E.O.-G.); fgomez@xochipala.com (F.G.-A.)
3 CRUST—Centro inteRUniversitario per l'analisi Sismotettonica Tridimensionale, 66100 Chieti, Italy
4 Seismological Research Centre, National Institute of Oceanography and Applied Geophysics (OGS), 34151 Trieste, Italy
5 IGG-CNR—Institute of Geoscience and Earth Resources, 56127 Pisa, Italy; m.laurenzi@igg.cnr.it
6 NORCE—Norwegian Research Centre, 5008 Bergen, Norway; wawh@norceresearch.no
7 Secretaría de Gestión Integral de Riesgos y Protección Civil Guerrero, Chilpancingo de los Bravo 39070, Mexico; snajerab@uvegro.edu.mx
8 Escuela Nacional de Estudios Superiores, Universidad Nacional Autónoma de México, Morelia 58341, Mexico; ajimenez@enesmorelia.unam.mx
9 GEOTOP & Département des Sciences de la Terre et de l'atmosphère, Université du Québec à Montréal, Montréal, QC H2X 3Y7, Canada; guevara_alday.jorge_alejandro@courrier.uqam.ca
10 IGG-CNR—Institute of Geoscience and Earth Resources, 50121 Florence, Italy; guia.morelli@igg.cnr.it (G.M.); andrea.orlando@igg.cnr.it (A.O.); giovanni.ruggieri@igg.cnr.it (G.R.)
* Correspondence: martina.zucchi@uniba.it

Abstract

The iron-oxide-copper-gold (IOCG) skarns of the Tatatila-Las Minas mining district in central Mexico represent a structurally-controlled, exhumed fossil geothermal system located in the eastern sector of the Trans-Mexican Volcanic Belt (TMVB). The district was historically exploited for gold and copper mineralization. The emplacement of the ore bodies was controlled by regional Neogene–Quaternary NE- and NW-striking fault systems formed during the extensional evolution of the TMVB. These faults acted as conduits for high-temperature hydrothermal fluids circulating during the cooling of the Neogene magmatic intrusions. By integrating detailed field study with available exploration borehole data, the spatial distribution of the skarn bodies was reconstructed. Three main emplacement geometries were identified: (a) at contacts between magmatic bodies and host rocks, (b) as lenticular or irregular bodies parallel to the host rock foliation, and (c) at the intersections of near-orthogonal faults. Although structural controls on skarn formation represent a key factor in ore emplacement, their analysis remains scarcely explored. This paper therefore contributes to filling this gap by providing a detailed characterization of the structural framework governing IOCG skarn development at Tatatila–Las Minas. The results improve understanding of IOCG systems formation and provide predictive criteria for mineral exploration in similar geological settings, potentially reducing exploration and mining risks.

Check for updates

Academic Editor: Changqian Ma

Received: 30 August 2025
Revised: 14 December 2025
Accepted: 17 December 2025
Published: 22 December 2025

Copyright: © 2025 by the authors. Licensee MDPI, Basel, Switzerland. This article is an open access article distributed under the terms and conditions of the Creative Commons Attribution (CC BY) license.

Keywords: IOCG skarns; extensional tectonics; exhumed geothermal system; Tatatila-Las Minas mining district; Trans-Mexican Volcanic Belt; structural controls; covellite Raman spectrum

1. Introduction

The Tatatila-Las Minas Mining District (Veracruz State in Central Mexico; Figure 1) is one of the most significant mining areas exploited in Mexico over recent decades. Skarn are key targets in mineral exploration because they commonly host economically relevant ore deposits (e.g., [1–4]); however, their evolution in relation to tectonic activity remains understudied. In particular, the structural control exerted by faults and fractures on skarn geometries is still poorly defined due to the limited number of documented case studies (e.g., [5–9]). The present work contributes to addressing this gap by analyzing an example in which regional fault systems played a primary role in skarn development. This district is located in the eastern sector of the Trans-Mexican Volcanic Belt (TMVB), which has been active since the early Miocene (e.g., [10–14]). Currently, the geothermal anomaly in this region is characterized by a heat flow of approximately 180 mW/m^2 and geothermal gradients consistently exceeding 70 °C/km [15]. Active geothermal systems aligned with the TMVB include, from west to east, Domo San Pedro, Cerritos Colorados, Los Azufres, Pathé and Los Humeros. Fossil geothermal systems have also been identified, exhumed after progressive cooling, uplift, and erosion of older magmatic bodies and associated contact metamorphic rocks (e.g., [16]). In some cases, these fossil systems serve as exceptional analogues for active geothermal fields. Among them, the Tatatila-Las Minas mining district can be considered a fossil exhumed analogue for the active Los Humeros geothermal field [17–21]) (Figure 1).

In this area, Miocene magmatism generated significant hydrothermal fluid circulation, inferred to be through secondary permeability (e.g., fractured rock volumes). This promoted fluid-rock interaction with the Mesozoic sedimentary host rocks, resulting in widespread mineralization [22,23], prominently exposed as iron-oxide-copper-gold (IOCG) ore bodies.

Cu-rich deposits are known to form in different tectonic settings, including continental and oceanic arcs (e.g., [24–26]), collisional orogenic belts (e.g., [27,28]), and continental areas affected by extensional tectonics (e.g., rift areas [5,29–31]). In extensional settings, the cooling of felsic magmas is often accompanied by large volumes of hydrothermal fluids (e.g., [6,32]), which migrate through permeability controlled mainly by faults and related fracture systems. Although metasomatic and mineralization processes leading to the formation of the IOCG deposits have been extensively documented worldwide (e.g., [31,33–38]), the structural mechanisms that regulate fluid circulation and mineralization are still not fully constrained, and fluid-rock interaction during their formation (e.g., [39,40]) remains poorly understood. Indeed, only a few studies have addressed how faults and fractures influence IOCG formation during magma cooling (e.g., [5,6,41]). Therefore, understanding the interplay between faults, fractures, geothermal fluid flow, and ore genesis is crucial for refining mineral exploration strategies and reducing mining-related risks. This also applies to the Tatatila-Las Minas area, where IOCG deposits have been characterized in detail from a mineralogical and petrographic perspective, including in recent studies [42], confirming their genetically link to the emplacement of Miocene intrusive rocks in the eastern sector of the TMVB [10–13,43]. However, their structural context, the processes responsible for their formation, and the geometry of the resulting skarn bodies had not yet been investigated.

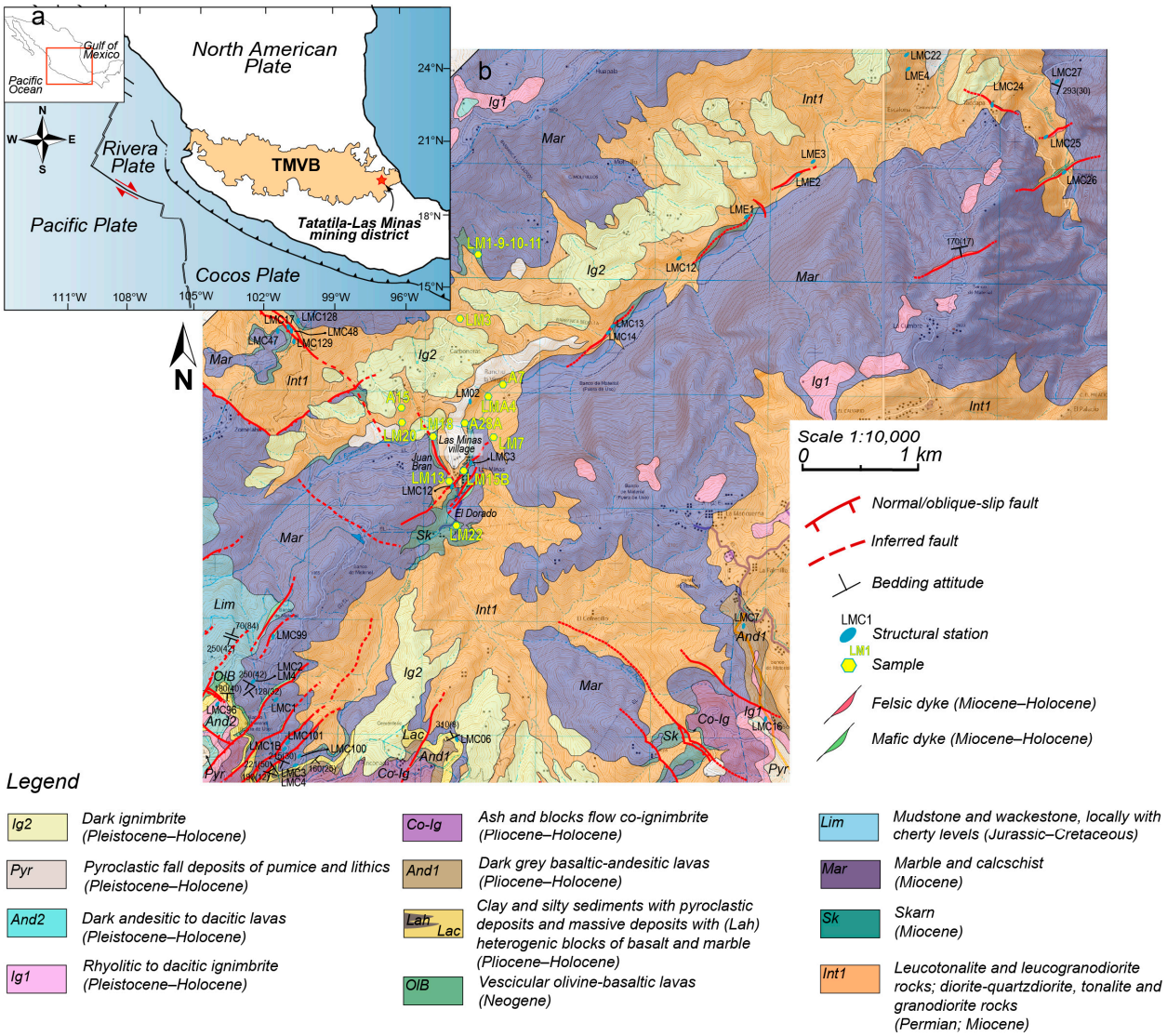

Figure 1. (**a**) Tectonic sketch map showing the Trans Mexican Volcanic Belt. The red star indicates the study area; (**b**) geological map of the Las Minas mining district (modified after [16]). The locations of the samples studied and the structural stations are shown on the map.

For this reason, this area represents a case study, where through a multidisciplinary approach (i.e., structural, petrographic and mineralogical analyses), we sought to address the lack of data regarding the geometry of these skarn bodies and to elucidate how their formation was controlled by circulation of hydrothermal fluids along fault zones. Our analysis shows that regional fault systems acted as the main conduits for hydrothermal fluids, allowing the skarn bodies to develop with different geometries and under varying geological conditions.

Our main results provide insights into the formation and spatial distribution of these ore deposits within the geological evolution of the TMVB, and are applicable to analogous geological settings characterized by extensional tectonics and contemporaneous magmatism.

2. Geological Framework

The Trans-Mexican Volcanic Belt is a Neogene–Holocene volcanic arc located in central Mexico (Figure 1a). This continental volcanic arc extends approximately 1000 km in a WNW-ESE orientation, and it is characterized by volcanic products ranging from mafic to felsic compositions. This arc is associated with the subduction of the Pacific Plate beneath

the North American Plate along the Mexican Pacific trench [11,12,14,43–45]. Volcanic activity along the TMVB can be divided into at least four main episodes, spanning from the early Miocene to the present [14,17,18,23,44,46,47]. In detail, the first episode (~21–10 Ma) referred to the TMVB formation as an east-west volcanic arc during the middle Miocene, with initial activity near the current volcanic front. Between ~13 and 10 Ma, volcanism migrated farther from the trench, forming stratovolcanoes and lava cones across central Mexico. The second episode (~11–6.5 Ma) involved a northward and eastward shift of mafic volcanism, forming widespread basaltic plateaus with both subduction-related and intraplate signatures. This episode marked a significant change from the earlier arc volcanism. The third period (~7.5–3 Ma) was characterized by decreased activity and the emergence of silicic volcanism. Mafic to intermediate lavas from the late Miocene to early Pliocene are interbedded with ignimbrites, showing a continued bimodal volcanic pattern. The fourth episode (since ~3.6 Ma) marked a transition to basaltic-andesitic arc volcanism and renewed intraplate activity, with widespread monogenetic fields and Quaternary stratovolcanoes dominating the western and central TMVB, while eastern sectors reactivated after a volcanic hiatus [14,17,18,23,44,46,47].

The hydrothermal mineralization and consequent skarn formation in the Tatatila-Las Minas area was related to the first magmatic episode (early to late Miocene) during the evolution of the TMVB, which in this eastern sector gave rise to intrusions emplaced into the Mesozoic sedimentary rocks of the Sierra Madre Oriental Province [14,17,43].

The eastern sector of the TMVB, where the study area is located, has been affected by two major fault systems (SW-NE and NW-SE) since the middle Miocene [13,17,48,49]. From the Pliocene onwards, NW-SE oriented intra-arc extension became dominant and affected the TMVB. This tectonic regime favored the development of normal fault striking SW-NE, WSW-ENE, and W-E, which controlled structural depressions [50–52] and volcanic alignments (e.g., volcanic edifices and eruptive centers) [49]. In this extensional context, NW-SE structures have been also reactivated [12,53,54], as evidenced by numerous volcanic alignments parallel to the NW-striking fault traces [49]. These relationships underscore the control exerted by major fault systems on the emplacement of magmatic bodies and eruptive edifices, thereby contributing to the development of a widespread geothermal anomaly characterized by heat flow values of about 180 mW/m^2 and geothermal gradients locally exceeding 70 °C/km [15], which favor the formation of extensive geothermal systems.

Over time, the large-scale circulation of hydrothermal fluids, attributed to the Miocene magmatic intrusions, promoted the ore-forming processes documented in the Tatatila-Las Minas mining district. This area is interpreted as an exhumed fossil geothermal system [16] and serves as a geological analogue of the nearby active Los Humeros geothermal field [18–21].

At the Tatatila-Las Minas area, Middle Miocene magmatism is represented by intrusive rocks with a composition spectrum from diorite to granodiorite understood as resulting from multiple magmatic pulses [55]. These intrusive bodies, together with dykes and sills, are considered the primary magmatic source of the hydrothermal fluids that reacted with the host rocks, resulting in widespread IOCG skarn formation [22,23]. Both dykes and skarn bodies were controlled by tectonic structures.

The skarn bodies are characterized by prograde and retrograde mineral assemblages and are classified as endoskarn and exoskarn types [42]. These formed at the interfaces between magmatic bodies (including sills and dikes) and the carbonate host rocks. The main skarn bodies include El Dorado, Juan Bran, Santa Cruz (Figure 1b), and Minillas, located north of the Las Minas village. Exploration data reveal that mineralization is often concentrated at the intersections of steeply dipping brittle structures cutting the host rocks. In other cases, the IOCG skarn bodies appear aligned along the primary discontinuities in

the host rocks (e.g., bedding), without a clear spatial association with magmatic intrusions (Figure 2; [56]). The skarns are primarily composed of garnet, with lesser amounts of pyroxene, epidote, and quartz, the latter likely representing a later hydrothermal stage [56].

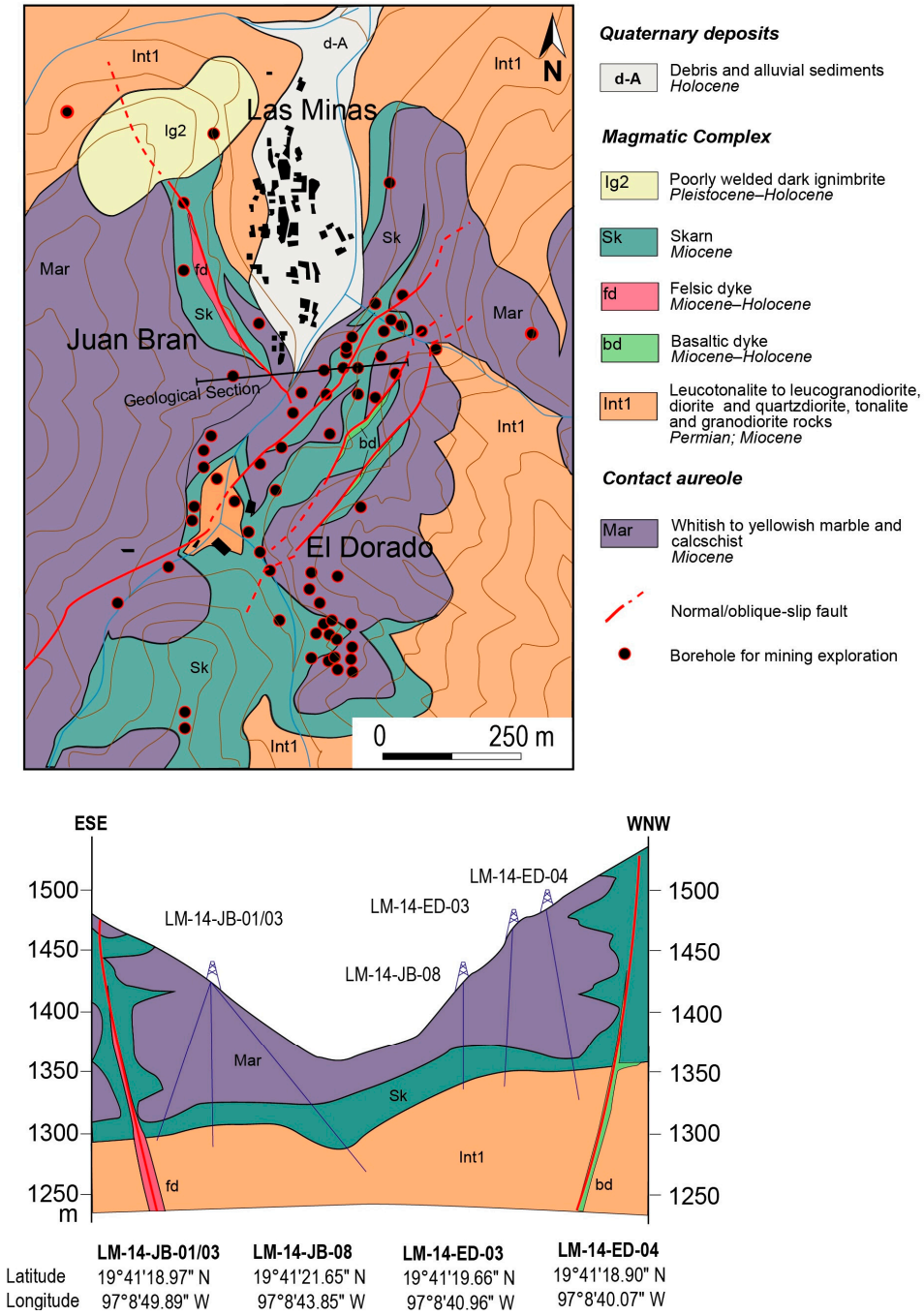

Figure 2. Tectonic geological map and related geological section (trace indicated on map) showing the relationships between IOCG skarn bodies and the main faults in the Tatatila-Las Minas area. Boreholes data are from [56].

3. Methods

The area surrounding the village of Las Minas was studied, with a focus on the Juan Bran and El Dorado skarn bodies (Figure 1b), which were explored and partially exploited during pre-colonial times [56]. Field mapping was integrated with structural and kinematic data to reconstruct the geometry and kinematics of faults. Samples of host rocks and IOCG deposits were collected throughout the study area and analyzed using optical microscope,

Scanning Electron Microscopy with Energy Dispersive Spectrometry (SEM-EDS), chemical, and electron microprobe (EMPA) analyses to characterize the mineral paragenesis and the petrographic features. The analytical procedures adopted in this study rely on standard instrument-specific reference materials and calibration routines that are conventionally used in laboratories operating the same equipment. These standards are those provided and validated by the instrument or by internationally recognized reference datasets.

SEM-EDS analyses were performed at the Department of Earth and Geoenvironmental Sciences, University of Bari (Bari, Italy), using a ZEISS EVO 50XPV instrument (Germany) equipped with X-max Silicon Drift (80 mm^2) detector (Oxford Instruments plc, UK) and a Super ATW (Super Atmosphere Thin Window). Operating conditions were 15.00 kV accelerating voltage and 800 pA emission current.

Seven selected fresh samples (Table S1 in Supplementary Material) from Miocene intrusive rocks were investigated for whole-rock major, trace, and REE elements at Activation Laboratories (Actlabs; Ancaster, Canada) by ICP-MS (codes 4LITHO and 4B2-std). For major elements, the precision (1σ) is estimated to be <2% for concentrations higher than 5 wt.%, and <5% for concentrations between 0.1 and 5 wt.%. For trace elements, the precision is 5% and 10% for the values in the ranges 1–100 ppm and 0.1–1 ppm, respectively. Whole-rock chemistries are provided in Table 1.

EMPA analyses were carried out at the laboratory of the National Research Council—Institute of Geoscience and Earth Resources (CNR-IGG) in Florence, Italy. The analyses utilized a JEOL JXA-8600 electron microprobe (Tokyo, Japan) equipped with four WDS spectrometers. The analytical parameters were as follows: 15 kV accelerating voltage, 10 nA beam current, and spot size of ~5 μm. Data collection accounted for the PAP model. These analyses were performed on samples LM10, LM15B, and LM18 (Table S1), which were prepared as 30-μm-thick polished thin sections. The results of the representative SEM-EDS and EMPA analyses are reported in Tables S2 and S3 (Supplementary Material).

Raman spectroscopy analyses were performed in order to identify opaque crystals with hexagonal habitus observed either as mineral inclusions within quartz and within fluid inclusions hosted in the same quartz. The Raman analyses were performed with a confocal Horiba Jobin Yvon Labram HR Evolution spectrometer at the Department of Earth and Geoenvironmental Sciences, University of Bari (Bari, Italy). The spectrometer is equipped with an Olympus optical microscope, a He-Ne laser source, and a multichannel air-cooled charge-coupled device (CCD) detector. A 50× long-distance objective was used, and the laser power was decreased to avoid potential local heating effects. The Rayleigh scattering component was removed by an ultra-low frequency (ULF) filter. Acquisition time (40–120 s) and number of accumulations (2–3×) were optimized to have the maximum spectrum intensity and to improve the signal-to-noise ratio. The spectral frequency was calibrated using the peak position (520 cm^{-1}) of a silicon fragment line of a Si wafer. Spectral processing (i.e., baseline subtraction, peak fitting) was conducted using the LabSpec 6 software package.

Four samples (three of intrusive rocks and one of skarn) were subjected to $^{40}Ar/^{39}Ar$ dating. Analyses were performed at the Ar-Ar laboratory of the Institute of Geoscience and Earth Resources (CNR-IGG) in Pisa (Italy), using analytical protocols described in [57]. Data were processed using ArArCALC software v.2.5.2 [58] and IsoPlot 3.0 [59]. Decay constants are those recommended by [60] and corrected in [61] for some updated physical constants. Displayed errors are at ±2σ level, unless otherwise stated; ages are reported with two errors, in the form ±X/Y. X is the analytical error linked to the measurement, which is used to compare ages within a sample. Y comprises the uncertainty on nuclear flux variation and is used to compare different samples. Further details on sample prepa-

ration are provided in the Appendix A, while the analytical data are reported in Table S4 (Supplementary Material).

Table 1. Major and trace elements composition of the intrusive rocks from the Tatatila-Las Minas area.

wt.%	Diorite to Quartz-Diorite				Tonalite		
	LM3	A15	A28A	LM20	LM13	LMA4	A7
SiO_2	52.91	55.74	56.10	56.90	58.59	59.80	60.78
Al_2O_3	18.34	17.13	16.97	16.41	16.63	17.07	16.76
Fe_2O_3	7.17	7.17	6.61	6.06	6.44	4.78	5.93
MnO	0.16	0.12	0.13	0.11	0.14	0.14	0.11
MgO	4.74	4.41	3.48	3.58	3.85	3.01	2.93
CaO	9.55	8.57	8.91	7.59	6.92	8.40	5.73
Na_2O	4.41	3.57	5.27	3.79	3.63	4.77	4.24
K2O	0.53	1.55	1.34	1.37	1.52	0.66	2.42
TiO_2	0.78	0.88	0.75	0.70	0.66	0.60	0.55
P_2O_5	0.24	0.25	0.29	0.16	0.19	0.22	0.20
L.O.I.	1.39	1.16	0.46	1.78	2.19	0.92	1.09
Total	100.22	100.55	100.31	98.45	100.76	100.37	100.74
ASI *	0.73	0.74	0.64	0.76	0.82	0.72	0.84
ppm							
V	207	199	127	161	177	144	124
Ba	257	421	619	356	505	357	669
Sr	627	662	593	526	467	562	442
Y	19	22	21	19	17	17	16
Zr	123	111	219	154	130	135	217
Rb	3	19	18	20	21	7	74
Nb	5	5	8	5	6	7	6
La	18.0	22.4	24.4	17.3	20.6	22.0	22.9
Ce	39.6	45.7	51.3	35.6	41.4	48.2	43.0
Pr	4.98	5.72	6.36	4.56	4.95	5.92	4.86
Nd	20.4	23.5	25.9	18.3	18.2	22.8	18.1
Sm	4.7	4.9	5.5	4.3	3.8	4.9	3.5
Eu	1.31	1.63	1.36	1.24	1.15	1.24	1.02
Gd	4.1	4.9	4.5	3.9	3.2	3.8	2.9
Tb	0.6	0.8	0.7	0.6	0.5	0.5	0.5
Dy	3.7	4.5	4.1	3.7	3.3	3.3	2.9
Ho	0.7	0.9	0.8	0.7	0.7	0.6	0.6
Er	2.1	2.4	2.3	2.1	1.9	1.9	1.7
Tm	0.3	0.36	0.34	0.31	0.26	0.26	0.26
Yb	1.9	2.3	2.1	2.2	2.1	1.7	1.8
Lu	0.29	0.32	0.31	0.34	0.3	0.26	0.29
Hf	2.6	2.8	4.8	3.7	2.9	2.9	4.8
Ta	0.4	0.4	0.4	0.4	0.6	0.6	0.5
Th	2.2	2.8	2.8	2.7	5.4	4.1	8.8
U	0.9	1.2	1.4	1.2	1.6	1.4	2.5

* Alumina Saturation Index = $[Al_2O_3]/([CaO] + [Na_2O] + [K_2O])$ molecular ratio.

4. Results

In the following, the presentation of data is separated into four different sections addressing the description of the stratigraphic setting and composition of Miocene intrusive rocks, faults systems, skarns and $^{40}Ar/^{39}Ar$ dating.

4.1. Stratigraphy and Miocene Intrusive Rocks in the Tatatila-Las Minas Area

The stratigraphic succession exposed in the study area includes rocks ranging in age from Jurassic to the upper Pleistocene, and can be divided into pre-volcanic units

and a volcanic succession. The pre-volcanic units consist of: (i) Paleozoic granitoids, dated at 268.14 ± 0.67 Ma by the $^{40}Ar/^{39}Ar$ method [22], with compositions varying from leucogranodiorite to leucotonalite. These rocks were later intruded by Miocene plutonic bodies consisting of diorite, quartz-diorite, tonalite, and granodiorite (Figure 3), dated at 14 Ma by the K/Ar method [22]; and (ii) Jurassic–Cretaceous carbonate rocks [16].

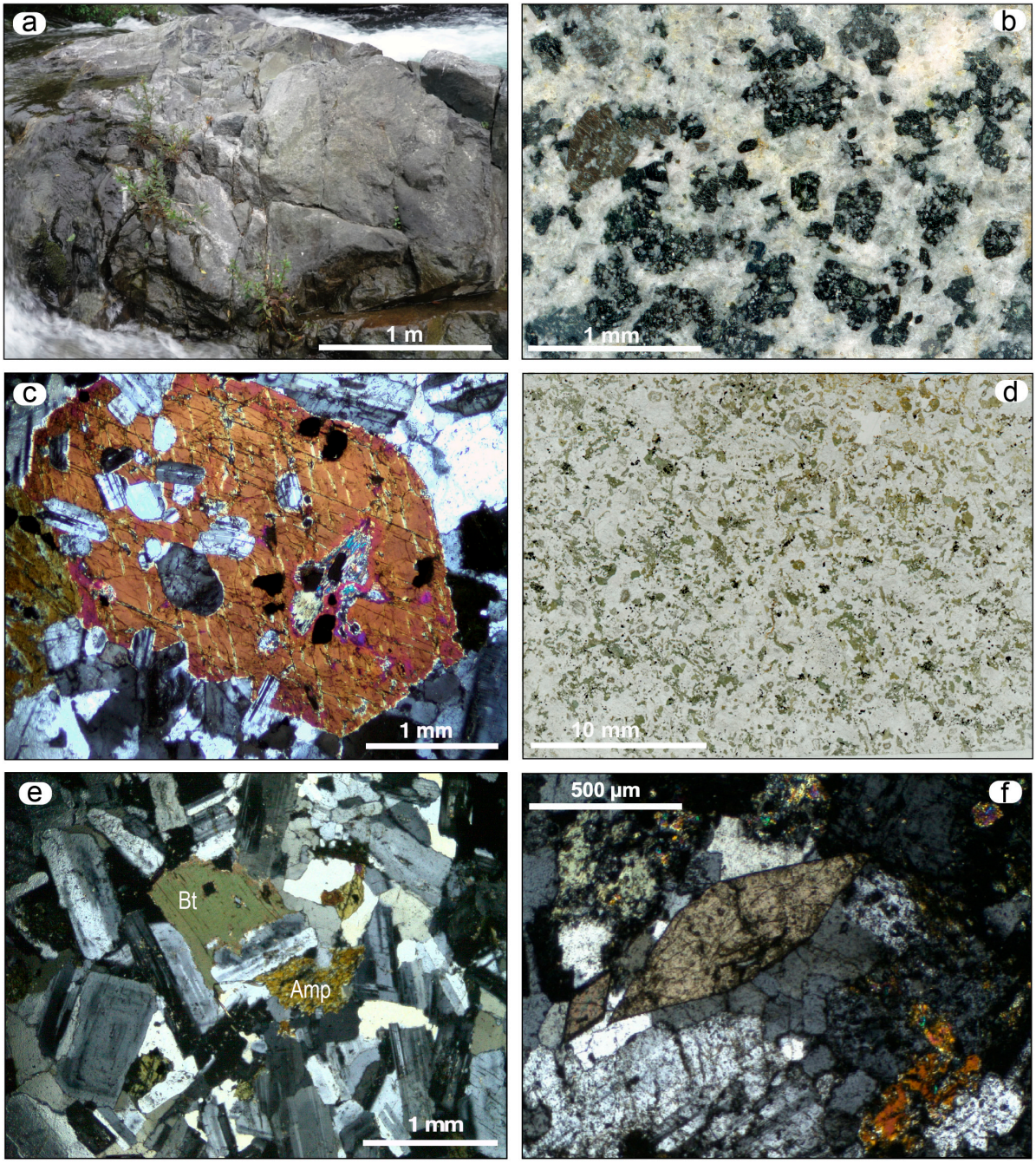

Figure 3. An overview of the Miocene intrusive rocks of the Las Minas area. (**a**) An outcrop of tonalitic to granodioritic rocks along the stream of Rancho la Virgen locality; (**b**) a picture of a small slab of diorite (sample A15) showing the mottled appearance of the rock, characterized by a texture with black amphibole oikocrysts enclosing numerous plagioclase chadacrysts; (**c**) micrograph of an amphibole enclosing several plagioclase chadacrysts, some uralitizated relicts of former clinopyroxenes and magnetite grains (crossed polars image); (**d**) thin section scan of a quartz-diorite (sample LM 13) showing a doleritic texture characterized by the abundance of plagioclase and amphibole, minor and

tiny biotite, and accessory magnetite (plane polarized light); (**e**) micrograph of tonalite (sample A7) showing the intergranular texture with zoned euhedral plagioclase and some biotite and amphibole crystals (crossed polars image); (**f**) micrograph of tonalite showing euhedral titanite grains, a common and accessory mineral in the Tatatila-Las Minas Miocene intrusive rocks (crossed polars image). Mineral abbreviations from [62].

The focus of this study is on the Miocene intrusive rocks with dioritic to tonalitic composition. In these rocks, amphibole and biotite are consistently present, except in one sample (A15), where biotite is absent and relics of former clinopyroxene are observed. The latter occurs as stubby inclusions within green-brown hornblende, largely replaced by actinolite and/or chlorite. Accessory minerals are mainly represented by magnetite, apatite, and titanite (Figure 3f).

In terms of rock texture, the more mafic rocks typically display a doleritic texture, characterized by randomly oriented, elongated plagioclase crystals showing oscillatory zoning (Figure 3e). Hornblende commonly occurs as oikocrysts enclosing smaller plagioclase crystals (Figure 3c). Both amphibole and biotite show evidence of alterations along cleavage traces, where the presence of chlorite ± calcite can be observed. Plagioclase frequently undergoes sericitization, particularly in the cores (Figure 3e), and it is rarely replaced by epidote.

The chemical composition of the main minerals of the four selected samples of diorite (A15), tonalite (A7), and quartz-diorite (LM13 and LM20) is reported in Table S2.

Plagioclase shows compositional zoning from labradorite-andesine in the cores to oligoclase at the rims in both diorite and tonalite. The analyses also indicate that amphibole can be classified as Mg-Hastingsitic hornblende, characterized by a moderately low aluminum content.

The major and trace elements composition of Miocene intrusive rocks is presented in Table 1. Diorite, quartz-diorite, and tonalite belong to the calc-alkaline to calcic magmatic series, indicating a syn-orogenic magmatic event. The alumina saturation index ASI (molecular ratio $Al_2O_3/[CaO + Na_2O + K_2O]$) points to the metaluminous nature of the rocks and tends to increase as silica increases. This may be due to fractional crystallization of amphibole [63], that together with plagioclase was mainly responsible for the magma differentiation.

The rare earth element (REE) patterns (Figure 4a,b) in the diorite to tonalite range are moderately fractionated, with an absent or weakly negative Eu anomaly. A closer inspection of the REE diagrams reveals that the tonalite exhibits a more evident concave-up pattern from Tb to Lu, which is also consistent with hornblende fractionation [63].

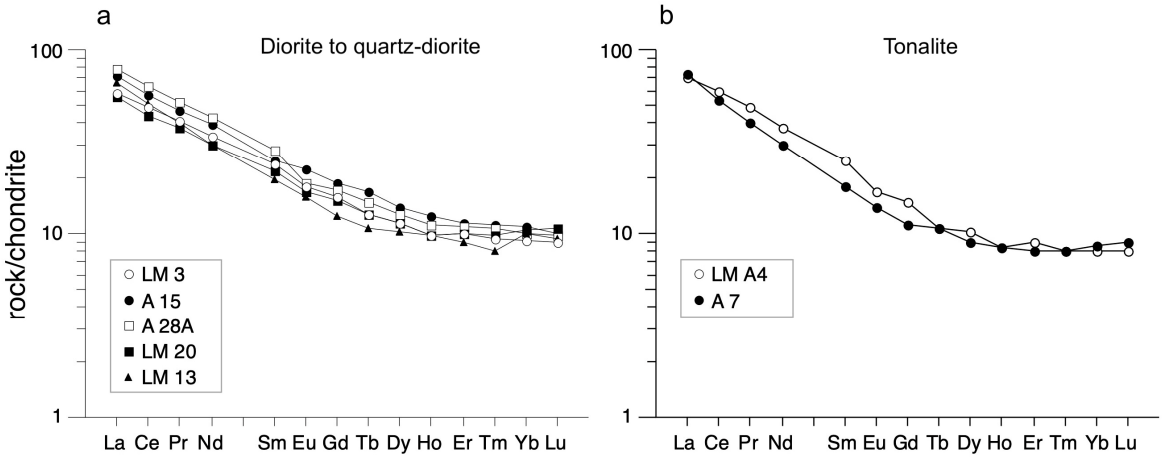

Figure 4. REE patterns for diorite to quartz-diorite (**a**) and tonalite (**b**). Chondrite normalizing values after [64]. REE analyses are reported in Table 1.

The intrusive complex is overlain by the host Jurassic–Cretaceous carbonate rocks, composed of limestone, with some layers having a dolomitic composition. The emplacement and cooling of the Miocene magmatic body promoted the development of a thermometamorphic aureole at the expense of limestone, resulting in marble. Marble may be of pure calcic or dolomitic composition, depending on the limestone layers involved.

A Neogene–Quaternary volcanic succession, associated with the TMVB (e.g., [11,44,47]) and specifically linked to the volcanic activity at Los Humeros, overlies the older units in an uneven manner. From bottom to top, this succession comprises Miocene olivine basalt lava and volcanic breccias, which are overlain by lacustrine sediments of Pliocene to lower Pleistocene age.

During the Quaternary, successive layers of andesite, ignimbrite, and pyroclastic fall deposits accumulated over this sequence. The deposits exhibit variable thickness and, in some cases, lateral compositional variations (i.e., ignimbrite deposits, lower Pleistocene). Felsic and mafic dyke swarms were emplaced in the intrusive complex and, to a lesser extent, into the overlying Pleistocene volcanic rocks. The felsic dykes range in composition from dacitic to rhyolitic, while the mafic dykes are basaltic. Their emplacement was structurally controlled by faults that remained active even after magma injection and cooling, as evidenced by the high density of fractures cutting across the dykes. Some of these fractures are also intersected by minor normal faults, indicating continued tectonic activity post-emplacement.

4.2. Fault Systems

Structural and kinematic data were collected at 86 stations across the study area, revealing two dominant fault systems, NE- and NW-trending (Figures 1b, 5 and 6), with map-scale lengths reaching up to 1.5 km. Although outcrops exposure is limited, the structural data strongly suggest that these fault systems played a significant role in the formation of the Las Minas valley and in controlling the emplacement of dyke swarms.

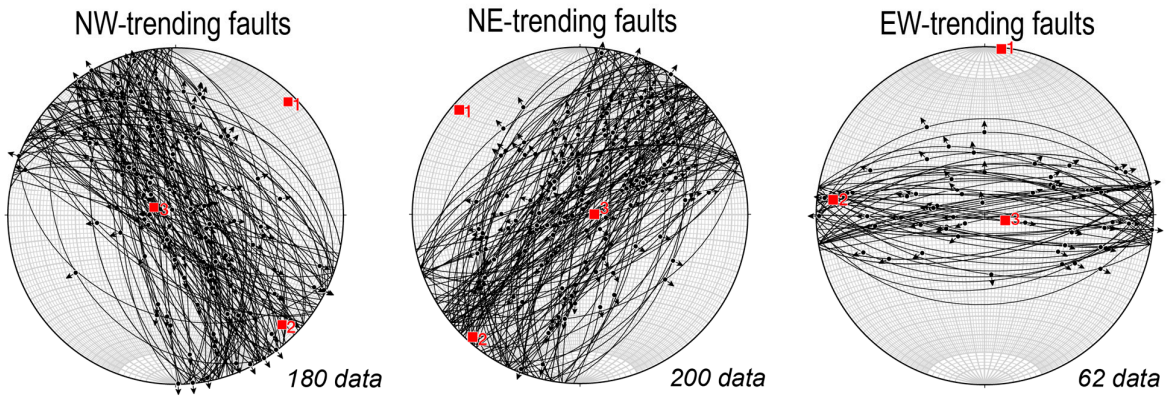

Figure 5. Stereographic diagrams (equal-area projection, lower hemisphere) illustrating faults and striae of the fault systems and related kinematic axes (red squares).

The geometric and kinematic characteristics of each system are summarized below:

(1) NE-trending fault system. This system is most prominent in the southwestern part of the study area and is characterized by fault damage zones up to 5 m wide, locally containing cemented tectonic breccias. It is also associated with minor WSW-ENE striking faults, which, together with NE-trending faults, form a conjugate fault system (Figure 5). Kinematic indicators on the slip surfaces include slickenfibers, mainly composed of calcite, and mechanical striations, which indicate dominant normal-slip kinematics, in places overprinted by minor oblique-slip movement (Figure 5). Maximum vertical displacements

along these faults reach approximately 70 m. In some cases, mineralization within the fault zones includes quartz veins up to 1 cm thick and disseminated pyrite.

(2) NW-trending fault system. It is characterized by slightly wider damage zones, reaching up to 8 m. Kinematic indicators, primarily mechanical striations on the slip surfaces, reveal a complex deformation history, including: (i) an initial strike-slip movement, followed by (ii) two phases of oblique-to-normal movements (Figures 5 and 6). The full fault zone width is rarely fully exposed due to dense vegetation; however, where observable, they consist of volumes characterized by dense networks and splays damage-rock that reflect the progressive development of the fault movement. These fractures contribute to enhanced secondary permeability within the fault zones, particularly at the intersections of the NE- and NW-trending systems. This increased permeability is especially evident south of Las Minas village, where the intersection of the two main fault systems coincides with the location of most significant skarn bodies: El Dorado and Juan Bran (Figures 1b and 2).

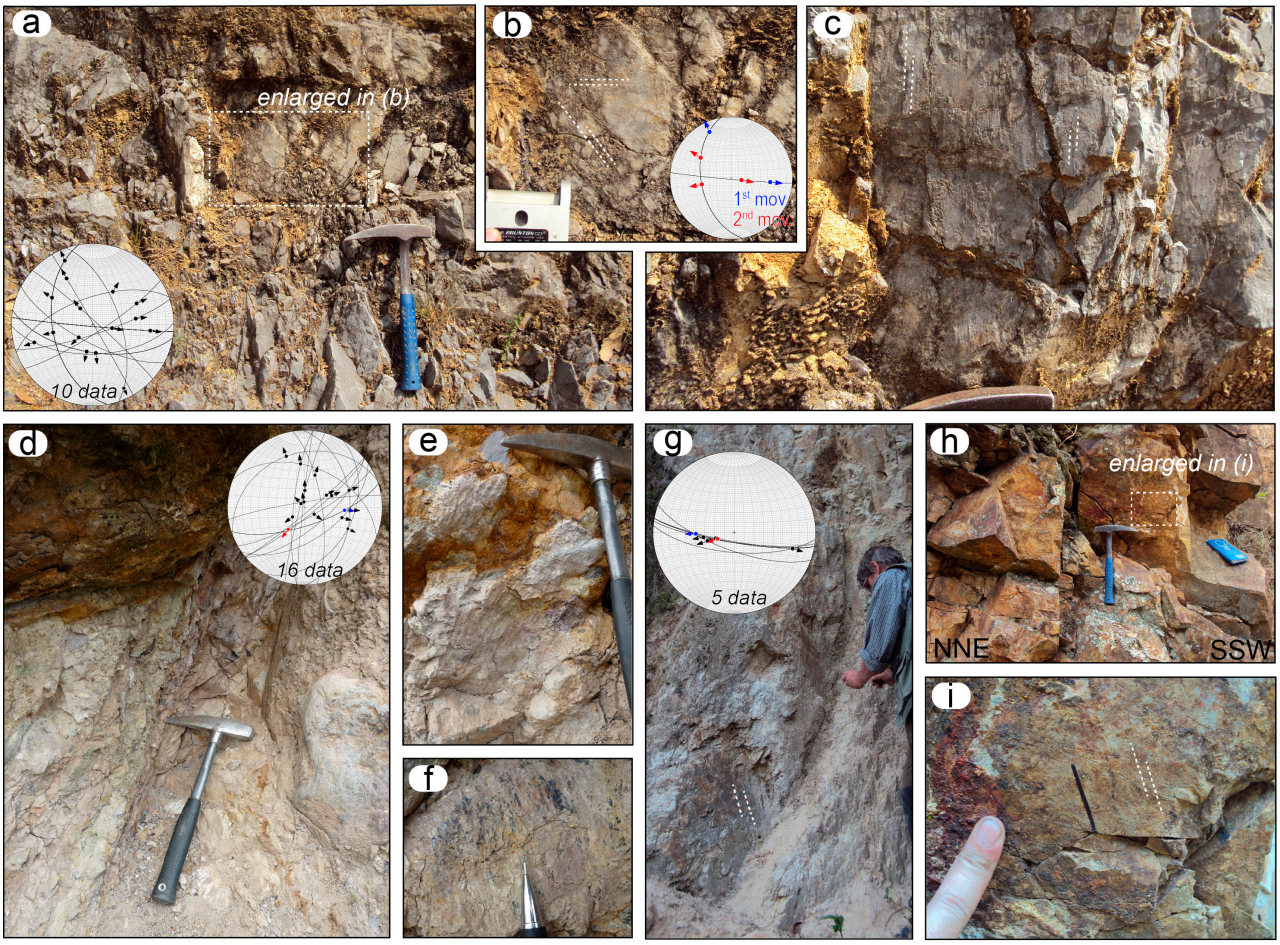

Figure 6. Examples of fault systems outcropping in the Tatatila-Las Minas area. (**a**) NW- and ENE-trending faults (structural station LMC1), the latter displaying in (**b**) two movements: a first left-lateral strike-slip (blue arrow on the stereoplot) overprinted by left-oblique-slip kinematic (red arrow on the stereoplot); (**c**) NE-trending fault characterized by mechanical striations indicating normal movement (structural station LMC1); (**d**) N-S and NE-SW trending faults with indication of hydrothermal fluid circulation (structural station LMC53); (**e**,**f**) details relating to the faults illustrated in (**d**), showing Fe-oxide and Fe-hydroxide (**e**) pervading the upper part of the picture, as well as evident kinematic indicators, which are mostly formed by mechanical striations, and syn-kinematic hematite fibers in (**f**); (**g**) NW-SE trending fault cutting carbonate rocks, with normal to right-oblique movement (structural station LMC27); (**h**) SW-NE trending fault plane and detail in (**i**) of kinematic indicators showing normal to oblique-slip movement (structural station LME1).

Fe-hydroxides are commonly observed on the slip surfaces of both NE- and NW-trending fault systems (Figure 6i), and in some cases, they also occur in localized zones within the broader fault damage zones. These features likely correspond to the most recent phases of fault activity. Widespread crosscutting relationships between NE- and NW-trending faults are throughout the study area, suggesting that both systems were active contemporaneously. This interpretation is also supported by the intrusion of both mafic and felsic dykes into the fault-damage zones, indicating syn-tectonic magmatic activity. The time span of fault activity is constrained by the presence of Pleistocene lacustrine sediments and volcanic units that are dissected by NE-trending faults, suggesting that deformation occurred from at least the Neogene to the Quaternary. These observations point to a prolonged tectonic evolution, during which faulting, magmatism, and hydrothermal activity were closely interrelated.

4.3. Skarn Bodies

Field observations and logs from mining-exploration boreholes indicate that the skarn bodies can reach thickness of up to 100 m (Figure 2). At the outcrop scale (Figure 7), they are easily recognizable by their bright colors, ranging from intense orange to red, attributed to the presence of garnet and metalliferous minerals (i.e., magnetite, bornite, chalcopyrite, pyrite), although the latter commonly appear weathered.

The presence of these metalliferous minerals increases the rock density, easily noticeable in the field when handling rock samples. In some case, the mineralized bodies are marked by bands of varying colors and composition, likely reflecting the composition of the protolith (Figure 7a,b). At the contact with the underlying intrusive magmatic rocks, the boundaries are typically irregular, marked by the occurrence of the endoskarn developed within the intrusive body, where the original igneous texture is completely overprinted. A sharp boundary is usually observable at the contact with carbonate rocks (Figure 7c,e). A detailed study on the skarn typology and mineralogical composition is provided by [42], to which the reader is referred for further information.

Overall, three primary structural settings for the skarn bodies have been documented through exploration drilling and field observations (Figures 2 and 7): (i) at the contact between the Miocene intrusive rocks and the host rock (marble; proximal skarn); (ii) as lenses within the marble, following the orientation of the main foliation (distal skarn); (iii) at the intersections of near-orthogonal faults with a sub-vertical attitude (distal skarn).

The two main skarn bodies in the study area, El Dorado and Juan Bran, were formed during the same mineralizing episodes taking place along the contact between intrusive and host rocks (Figure 1b). The skarn bodies are characterized by the presence of Au-Cu-(Ag)-magnetite mineralization, developed along the flat-lying roof of the Miocene intrusive rocks at the contact with marble. In addition, minor skarn bodies, typically with lenticular shape, are hosted within marble.

The geometry of the main skarn body, as reconstructed from boreholes south of Las Minas village, reveals a thickness locally exceeding 200 m (Figure 2; [56]). Borehole data also indicate that the mineralogical composition of the skarn, characterized by the presence of garnet and clinopyroxene, remains laterally consistent. The retrograde phase mainly consists of chalcopyrite (Figure 7h), which replaces magnetite, with or without bornite. Magnetite occurs in massive pockets or as sub-planar bodies characterized by centimeter-wide bands alternating with garnet-rich levels (Figure 7f). Less commonly, magnetite forms in irregular diopside-bearing bodies. Pyrite is rare and formed during the latest stages of skarn evolution (Figure 7g).

At the microscope scale (Figure 8), two distinct types of skarns can be identified: (i) clinopyroxene-dominated (Figure 8a,b) and (ii) garnet-dominated (Figure 8c).

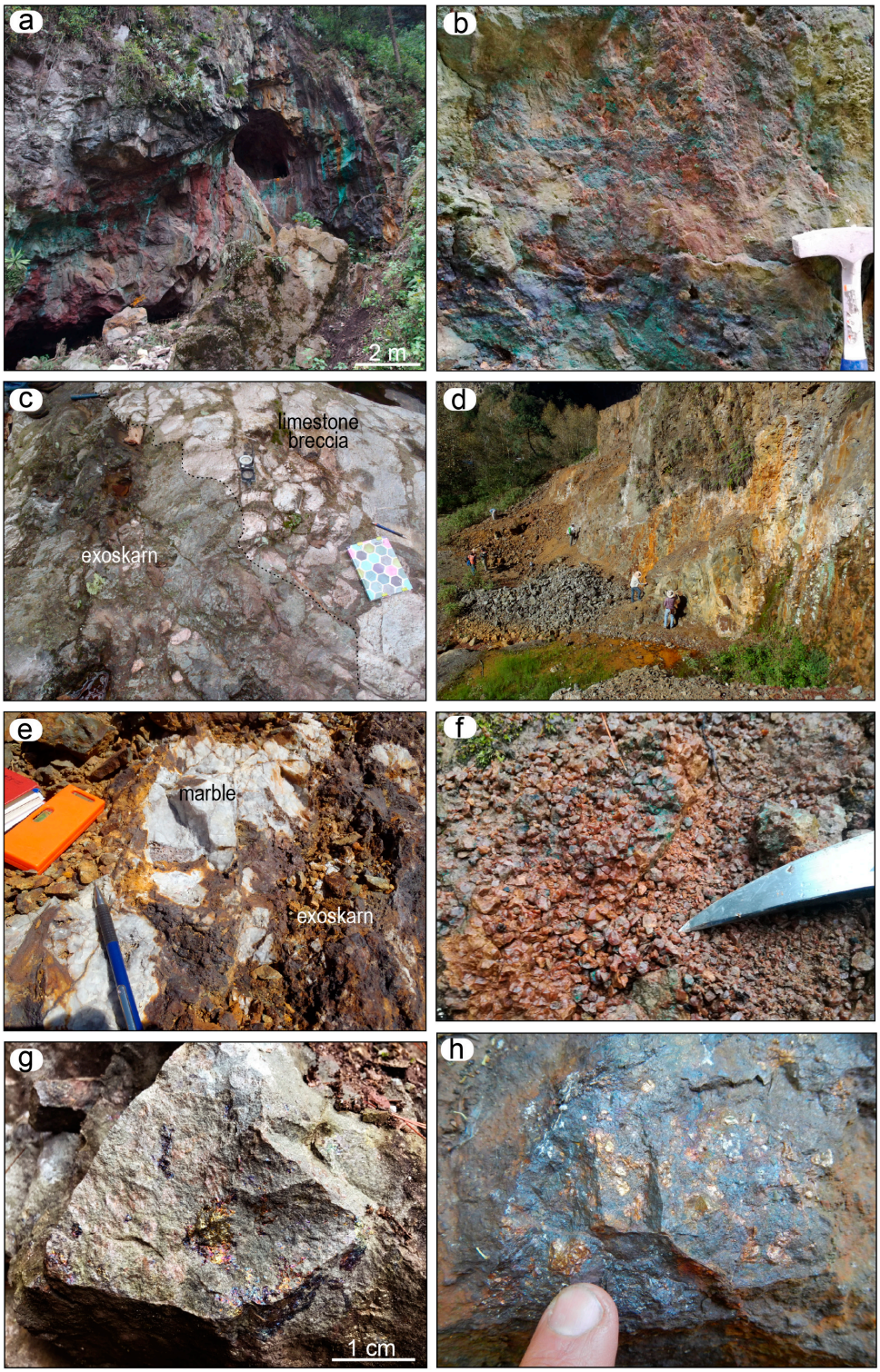

Figure 7. Examples of IOCG skarn at outcrop scale. (**a**) Skarn deposit cropping out at El Dorado area, showing bands of different colors and compositions; (**b**) a highly altered fault surface with quartz, malachite, and azurite in addition to Fe-hydroxides and oxides; (**c**) picture showing the contact between brecciated limestone and exoskarn; (**d**) panoramic view of metasomatic alteration in the Jurassic-Cretaceous carbonate rocks. The original bedding structure is maintained; (**e**) contact between marble and exoskarn; (**f**) garnet-rich skarn showing localized patina of malachite and azurite; (**g**) iridescent pyrite within a garnet-dominated exoskarn; (**h**) chalcopyrite mineralization.

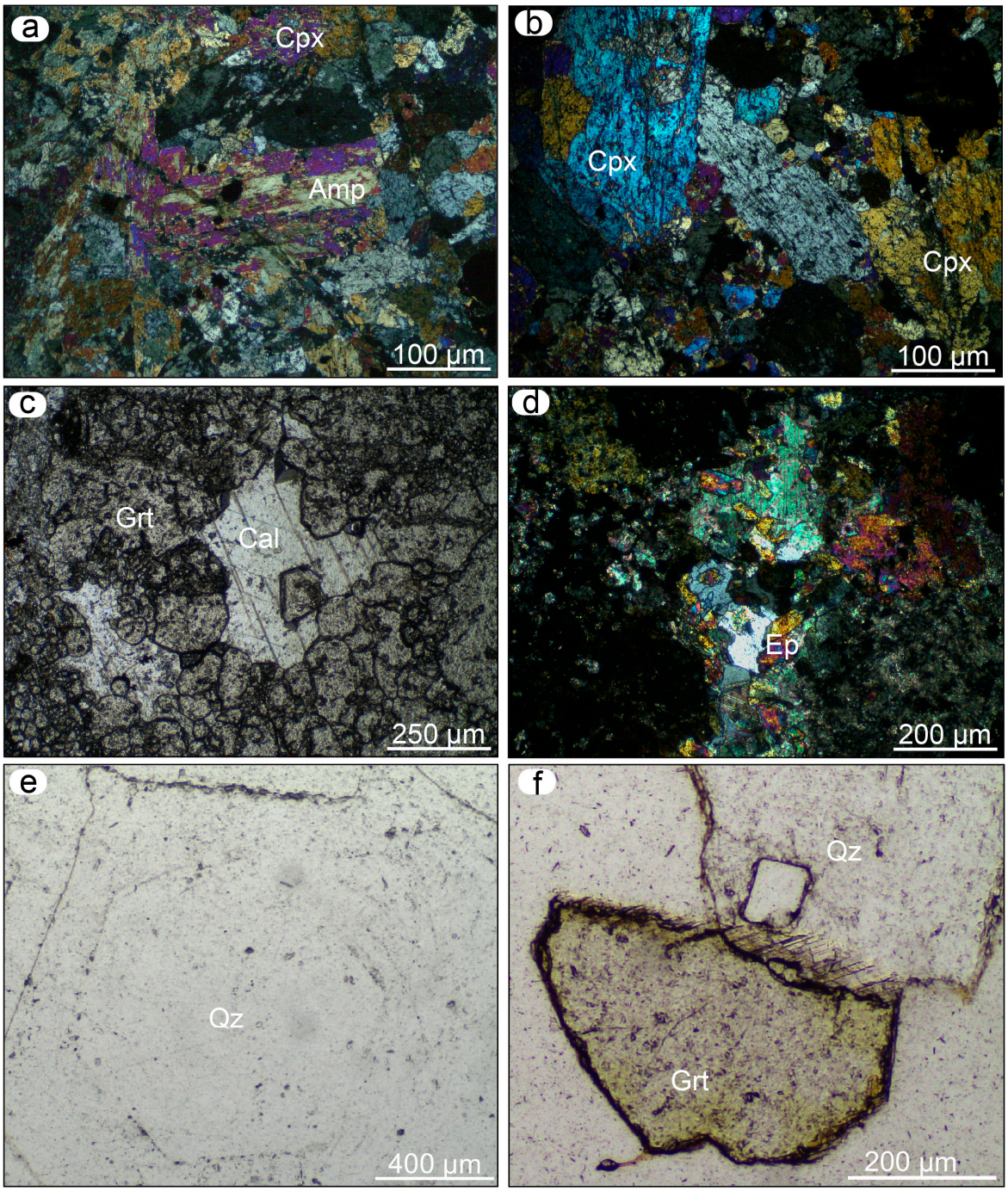

Figure 8. Representative optical micrographs of skarn. (**a**,**b**) Cpx-dominated skarn with Mg-Ca-rich amphibole (crossed polars); (**c**) Grt-dominated skarn (plane polarized light); (**d**) epidote crystals filling a vein (crossed polars); (**e**) image showing a quartz grain with hexagonal habit; (**f**) polysynthetic twinning zone in the quartz grain at the contact with garnet. Mineral abbreviation from [62].

SEM-EDS and EMPA analyses on both Cpx-rich and Grt-rich skarn samples were performed (Tables S1 and S3). Both types underwent a retrograde fluid circulation stage, which facilitated the formation of hydrous minerals such as amphibole, epidote, chlorite, and white mica, mainly observed within veins crosscutting the skarn bodies. In the Cpx-dominated skarn, the mineral assemblage includes anorthite + quartz + amphibole + magnetite + epidote + chlorite + pyrite ± chalcopyrite ± apatite ± titanite ± rutile, in addition to pyroxene with a diopside composition (Figure 8d and Table S1). Rare crystals of wollastonite are present. The amphibole belongs to the calcic group, primarily composed

of pargasite, Mg-hastingsite, and actinolite (Table S3). Amphibole typically forms at the expense of primary clinopyroxene during the retrograde cooling in the presence of H_2O. In the Grt-dominated skarn, the mineral assemblage consists of garnet + plagioclase + quartz + epidote + magnetite + calcite + pyrite ± chalcopyrite ± sphalerite.

The composition of garnet ranges from grossular-rich to andradite-rich content (Table S3). This compositional variability is reflected in SEM/BSE images (Figure 9a), where the crystal brightness change from dark to light grey with decreasing aluminum content. Late-stage epidote locally occurs in both skarn types as grains aggregates (Figure 8d) or as inclusions within quartz. Micro-fractures within garnet are sporadically filled by sulfide minerals such as sphalerite, chalcopyrite, and pyrite, along with calcite and quartz (Figure 9c).

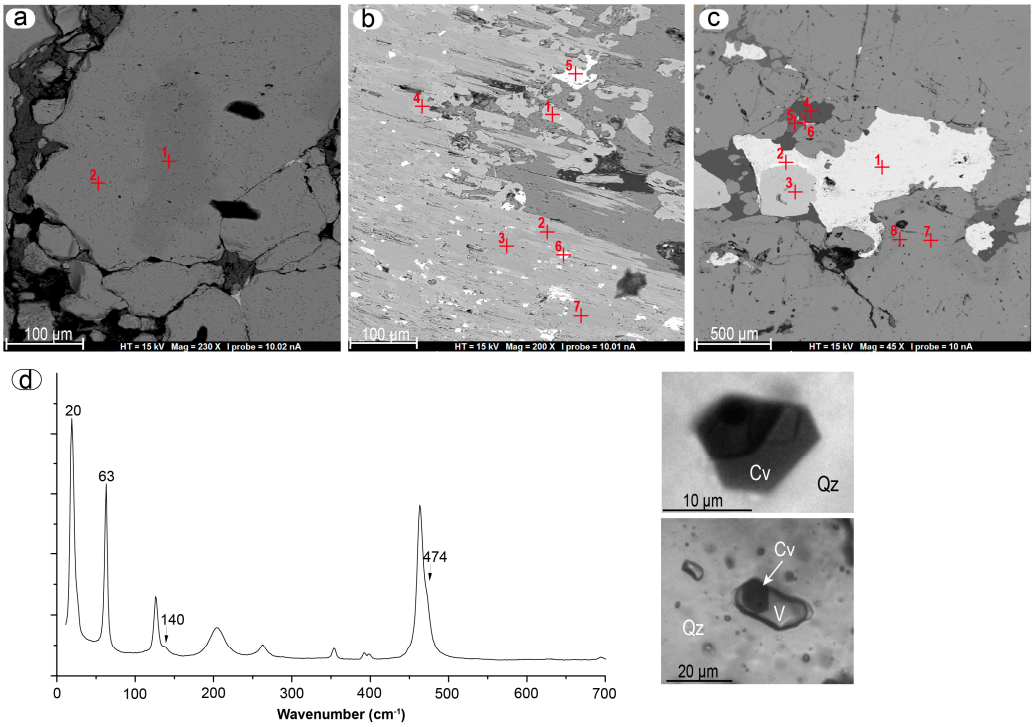

Figure 9. (**a**) Zonation in a garnet crystal with andradite-grossular garnet (point 1) bordered by an andradite-rich garnet (point 2) of LM18 sample (corresponding to points 1 and 2 of site 3 analyses in Table S3); (**b**) amphibole (points 3, 7, and 2, corresponding to point 2 of site 2 in Table S3), epidote (points 4 and 1, corresponding to point 1 of site 2 in Table S3), and magnetite (points 5 and 6) in LM 10 sample; (**c**) late stage chalcopyrite (point 1), sphalerite (point 2), pyrite (point 3), quartz (point 4), calcite (point 5), and bornite (point 6) filling cavities and fractures in andradite-rich garnet in LM 18 sample (points 7 and 8 of site 1 in Table S3). (**d**) Representative Raman spectra of hexagonal copper minerals (in micrographs) hosted in quartz and fluid inclusions (V = vapor phase). Mineral abbreviation from [62].

Quartz occasionally exhibits a hexagonal habit with distinct zoning growth (Figure 8e). Furthermore, polysynthetic twinning is locally observed in quartz margin at the contact with garnet (Figure 8f), likely related to the α-β quartz phase transition, which typically occurs at 573 °C [65–67]. SEM/BSE observations also reveal the presence of magnetite as dispersed grains, ranging in size from a few to hundreds of microns, within the skarn assemblage (Figure 9b).

A patina of malachite and azurite covers the skarn surface, along with sulfides that are easily recognizable in the field (Figure 7b). These sulfides are sometimes recognizable at micro-scale. Indeed, small crystals measuring up to 10 µm and exhibiting a hexagonal habitus with colors ranging from blackish to pale green, were identified within hydrother-

mal quartz associated with sulfides in one sample (LM1; Figure 1b and Table S1). Similar crystals were also observed in few vapor-rich fluid inclusions hosted in the same quartz (Figure 9d). The non-systematic occurrence of such crystals in vapor-rich inclusions and their presence within quartz suggest that they were transported by the fluid precipitating quartz and that they were accidentally trapped within fluid inclusions (i.e., they are not daughter minerals) [68,69]. Micro-Raman spectroscopy identifies these minerals as covellite, on the basis of literature data and factor group analysis [70,71]. Indeed, according to the factor group analysis, a Raman spectrum of covellite should consist of eight Raman active phonon modes: two totally symmetric (A1g), two doubly-degenerate (E1g) and four doubly-degenerate (E2g) phonon modes. Of these, about six bands are generally observed in the frequency region below 500 cm^{-1}, three intense phonon modes around 19, 62, and 475 cm^{-1}, and three weaker bands at 112, 142, and 267 cm^{-1} are typically observed in the Raman spectra of CuS. The modes near 19 and 475 cm^{-1} are assigned to vibrational modes from the covalent S−S bonds. The other modes are generally assigned to bending and lattice vibrational modes [70,71].

Figure 9d displays the Raman spectrum matrix in the frequency region of 10–700 cm^{-1} for the hexagonal solid inclusion enclosed within the quartz crystal. The very sharp and intense Raman peaks observed around 20 and 63 cm^{-1} in the low-frequency region can be clearly attributed to a CuS phase. A third Raman phonon mode characteristic, at about 475 cm^{-1}, appears as a shoulder of the intense band at 465 cm^{-1}, which is associated with the quartz matrix. Moreover, the Raman spectrum also revealed, in the low-frequency region, a weak peak around 140 cm^{-1}, which is also attributed to the covellite phase.

4.4. $^{40}Ar/^{39}Ar$ Dating

Three samples of intrusive rocks (LM13, LM20 and A15) and one skarn (LM22) were analyzed for $^{40}Ar/^{39}Ar$ dating (Figure 1b and Table S1). Sample LM13 (an amphibolic quartz-diorite with medium-fine grain size and doleritic structure) has a discordant age spectrum, with high ages at initial (low temperature) steps, followed by a slight wavy trend for the following ten intervals (Figure 10(A-a)). The three initial steps have very low ^{40}Ar yields and contain more than two thirds of the atmospheric Ar content of this sample (Table S4); the presence of secondary alteration phases is the most likely cause. Neglecting the first two steps, which contain only about 2% of ^{39}Ar release, either K/Ca and K/Cl spectra are saddle shaped (Figure 10(A-b,A-c)). This sample does not identify a statistically significant plateau and/or isochron age. Six steps (red line in Figure 10(A-a)) with the lowest K/Ca and K/Cl ratios have a weighted average of 14.04 ± 0.43 Ma [MSWD = 9.29], and a simple average that is very close, 13.98 ± 0.52 Ma. The step with the lowest K/Ca and K/Cl ratio, near to micro-analytical data (Table S2), has a datum of 14.69 Ma, which can be considered an estimate of this sample age. The integrated total age is 14.86 ± 0.19 Ma (Table 2).

Amphibolic diorite LM20 (heterogeneous grain size and doleritic structure) has a saddle shaped age spectrum, with old ages on low and high temperature steps, and no statistically significant plateau age can be derived (Figure 10(B-a)); in this case, the age of the youngest step, 15.49 Ma, is considered a maximum age for the sample. However, irregular age spectra can also be caused by the presence of parentless ^{40}Ar in the sample, not derived from in situ ^{40}K. The age calculation routine of individual steps assumes an atmospheric $^{40}Ar/^{36}Ar$ initial isotopic ratio (298.56), and step ages are used to calculate the plateau age. On the contrary, the isochron approach does not make any assumption on the initial Ar isotopic composition of the sample, so isochron ages, when computable, are automatically corrected for the initial ratio. In our case, eight steps, corresponding to 76.9% of ^{39}Ar release, identify an isochron age of 15.11 ± 0.39/0.40 Ma (MSWD = 1.2), with

a radiogenic $^{40}Ar/^{36}Ar$ initial isotopic ratio (345 ± 11) (Figure 10(B-d) and Table S4). The integrated total age is much older than isochron age, 19.30 ± 0.23/0.25Ma. K/Ca and K/Cl spectra are saddle shaped, as is the age spectrum (Figure 10(B-b,B-c)). High K/Ca and K/Cl ratios in the initial intervals might be due to the presence of alteration phases that melt at low temperature and/or to fluid inclusions.

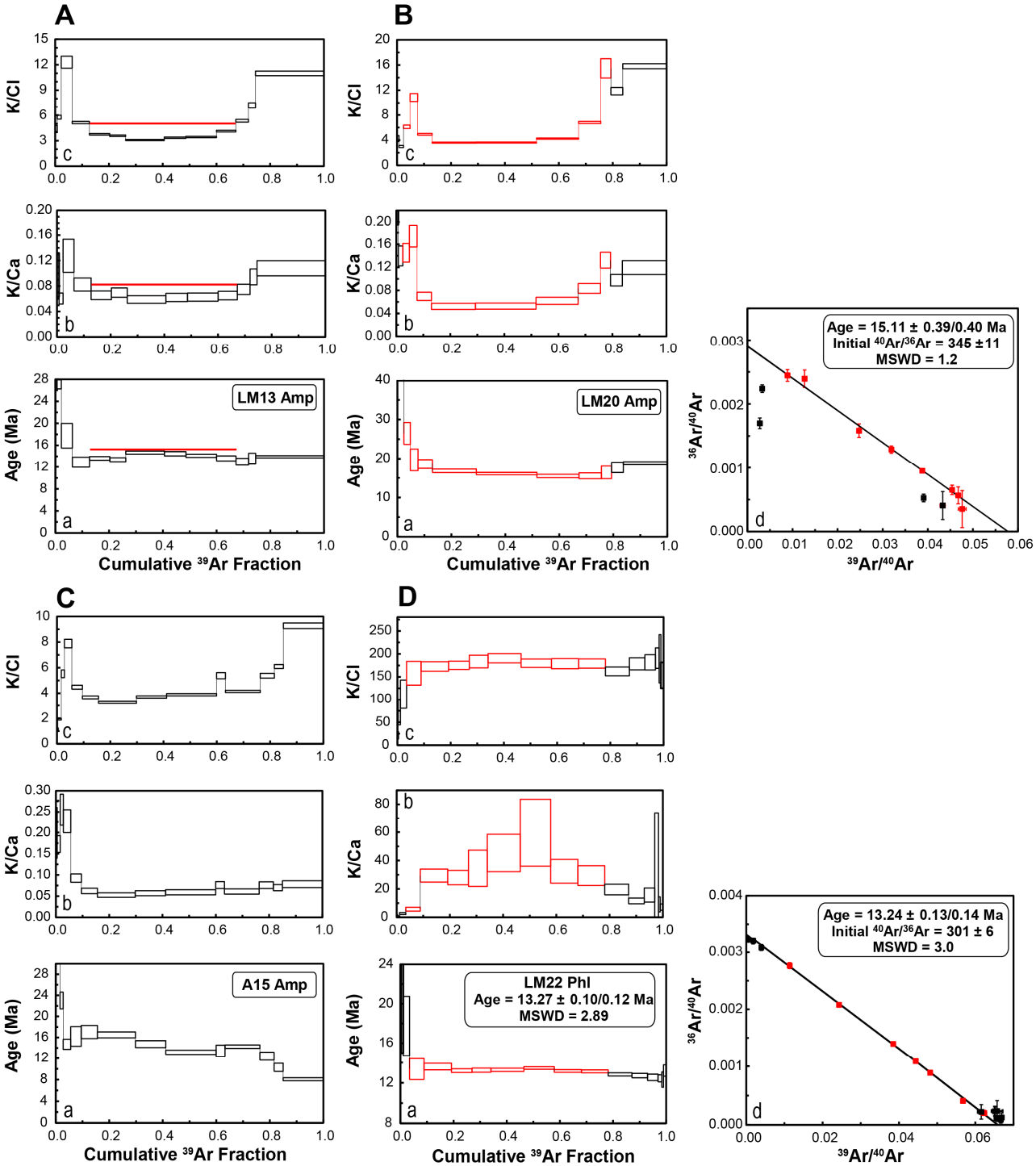

Figure 10. (**A**) Age (a), K/Ca (b), and K/Cl (c) spectra of LM13 Amp; (**B**) age (a), K/Ca (b), K/Cl (c) spectra and inverse isochron plot (d) of LM20 Amp; (**C**) age (a), K/Ca (b), and K/Cl (c) spectra of A15 Amp; (**D**) age (a), K/Ca (b), K/Cl (c) spectra and inverse isochron plot (d) of LM22 Phl. Data points used to calculate plateau and isochron ages are in red; MSWD: mean standard weighted deviates. Errors are at the 2σ level. For details see main text.

Table 2. Summary of $^{40}Ar/^{39}Ar$ ages. Preferred ages are in bold.

Sample	Phase	% ^{39}Ar	Age (pl)	±2σ	MSWD	Age (is)	±2σ	MSWD	$^{40}Ar/^{36}Ar_{in}$	TF Age	±2σ
			Ma	Ma		Ma	Ma			Ma	Ma
LM22	phl	74.7	**13.27**	**0.10/0.12**	2.89	13.24	0.13/0.14	3.0	301 ± 6	13.50	0.14/0.15
LM20	amp	76.9	–			**15.11**	**0.39/0.40**	1.2	345 ± 12	19.30	0.23/0.25
LM13	amp		–			–				14.86	0.19/0.20
A15	amp		–			–				14.09	0.20/0.21

Notes: % ^{39}Ar = percentage of ^{39}Ar released used for plateau or isochron age calculation; pl = plateau age; MSWD = Mean Squared of Weighted Deviation; is = isochron age; $^{40}Ar/^{36}Ar_{in}$ = initial $^{40}Ar/^{36}Ar$ ratio; TF = total fusion age; see text for the degree of error. Mineral abbreviations from [62].

Amphibole A15 exhibits a highly irregular age spectrum, characterized by a stair-case drop in age from the first to the last step (Figure 10(C-a)). While the overall shape may suggest ^{39}Ar recoil, the sample is not fine grained; instead, it contains several small plagioclase inclusions that are difficult to completely remove. Assessing the contribution of plagioclase to the age spectrum is challenging due to its compositional zoning, and because the bulk K/Ca ratio is not significantly different from that of amphibole. The K/Ca spectrum, starting from 10% of ^{39}Ar release, is relatively flat, with a slight positive slope (Figure 10(C-b)), whereas the K/Cl spectrum displays a saddle-shaped profile (Figure 10(C-c)).

No amphibole analyzed in this study yielded a flat, undisturbed age spectrum, despite careful mineral separation procedures. As highlighted in Section 4.1, the amphiboles commonly contain plagioclase inclusion and exhibit evidence of alteration, which likely account for the irregularities observed in the age, K/Ca, and K/Cl age spectra.

Phlogopite LM22, from a calc-silicatic vein of skarn, shows an age spectrum characterized by elevated apparent ages at low-temperature steps, a relatively flat central portion, and slightly younger ages at higher-temperatures steps, with the exception of the final fusion step. The low-temperature steps are significantly enriched in atmospheric Ar. Eight steps, comprising almost 75% of ^{39}Ar release, give a plateau age of 13.27 ± 0.10/0.12 Ma with a high MSWD (2.89) (Figure 10(D-a)), while the integrated total age is subtly older than the plateau age, 13.50 ± 0.14/0.15 Ma. The isochron age calculated on the eight steps is 13.24 ± 0.13/0.14 Ma (MSWD = 3.0), overlapping within error with the plateau age, and with an initial $^{40}Ar/^{36}Ar$ isotopic ratio (301 ± 6) atmospheric within error (Table 2 and Figure 10(D-d)). The K/Ca ratio displays a wide interval of values (0.7 ÷ 60) for a sample devoid of Ca, with the lowest values in the initial and final steps (Figure 10(D-b)); one reason is the likely presence of carbonatic impurities in mica crystals. The K/Cl ratio remains relatively constant throughout the experiment (Figure 10(D-c)).

5. Discussion

5.1. Tectonic Setting and Control on Skarn Formation

Skarns are bodies formed through the metasomatic replacement and chemical alteration of their protoliths [1,3,72–79]. They represent key exploration targets during mining activity due to their enrichment in metallic elements. However, skarn bodies typically exhibit irregular geometries, making them difficult to predict [8,80–82].

Generally, skarn bodies can be observed in four primary settings: (i) along the contact between intrusive magmatic bodies and host rocks; (ii) as lenticular or irregular bodies aligned with the primary foliation of the host rocks; (iii) as irregular bodies cross-cutting geological boundaries and host-rock foliation; or (iv) associated with major faults and/or fracture systems (Figures 1b, 2 and 7). However, direct structural evidence can be obscured when the original permeable faults, fractures, or strata that channeled the metasomatizing

fluids are no longer preserved—either sealed by mineral deposits or entirely replaced by skarn mineralization.

In the Tatatila-Las Minas area, at least three geometrical configurations have been observed in the field and reconstructed from borehole data (Figure 2), highlighting a strong spatial association between skarn formation and structural and/or lithological discontinuities. Specifically: skarn body developed (i) at the contact between Miocene intrusive rocks (as massive bodies and dykes) and marble; (ii) as secondary lenses formed within the marble, in which their shape was controlled by bedding or pre-existing anisotropies; and (iii) at intersections between NE- and NW-striking faults, where damage zones enhanced secondary permeability. From this, it can be inferred fault zones and the presence of pre-existing permeable discontinuities, such as lithological boundaries and foliation, played a key role in controlling the circulation of hydrothermal fluids and the formation of the El Dorado and Juan Bran skarn bodies. The lateral dispersion of fluids away from the fault zones led to the development of intra-block skarn volumes parallel to bedding and/or foliation, as observed in outcrop and indicated by the mining-exploration borehole logs.

Accordingly, a conceptual model for skarn distribution is presented in Figure 11. Based on this, the intersection of the NW- and NE-striking faults likely explains the localization of the main ore-bodies (El Dorado and Juan Bran) just south of Las Minas village, where fault intersections are prominent. On the other hand, the role of fault zones in controlling hydrothermal fluid circulation has been widely recognized by several authors (e.g., [83–87]) and well documented in both active (e.g., [88–95]) and inactive (i.e., fossil) geothermal systems (e.g., [96–98]).

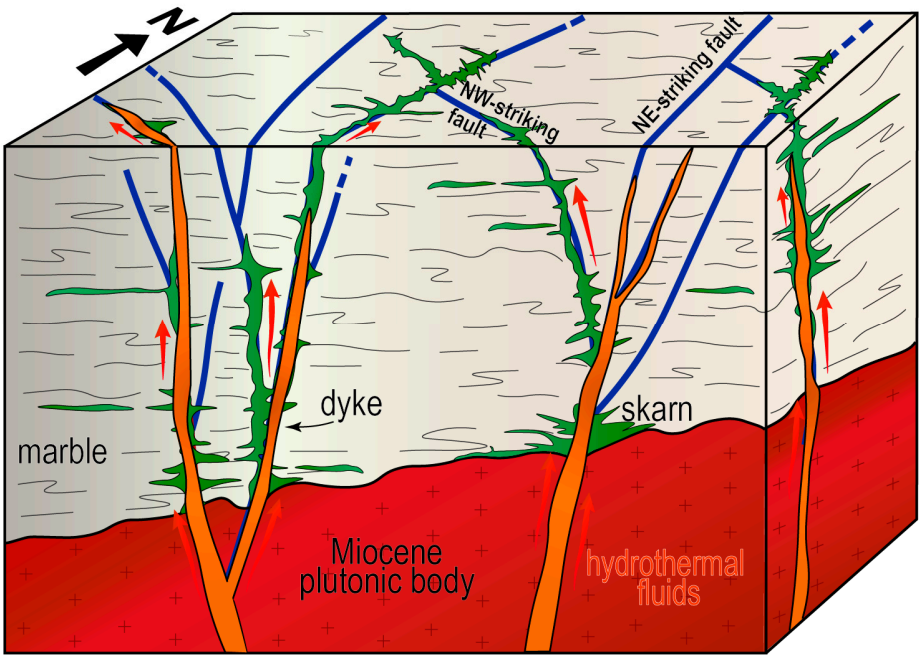

Figure 11. Conceptual model (not to scale) showing the relationships between the two main fault systems (blue lines), dykes (in orange color), hydrothermal fluids (red arrows) and the development of skarn bodies (in green color), whose geometries were partly controlled by faults and partly by stratigraphic unconformities.

In the Tatatila-Las Minas area, the described fault systems were active contemporaneously between Miocene and Pleistocene, with faulting ending prior to the deposition of youngest volcanic deposits, which are not involved in the deformation [16]). We interpret their kinematic relationship within a common extensional stress field dominated by NW-trending extension [13,16,99,100]. Their mutual orthogonality is consistent with an

extensional regime, where NW-striking faults acted as transfer structures accommodating the normal or oblique-slip movements along the NE-striking normal faults.

The final movements of both fault systems were marked by dominant normal displacements, likely driven by regional uplift associated with high surface heat flow. In this context, the pre-existing fractured volumes, representing weakened sectors, were reactivated as normal faults regardless of their original orientation. Similar structural evolution has been documented in other extensional tectonic settings [92,101,102].

Overall, permeability was primarily controlled by the orientation of the intermediate principal stress axis and by the connectivity of fracture networks formed at the intersection between the two fault systems [85,103]. In this framework, NW-SE faults channeled deep geothermal fluids toward shallow crustal levels, which then migrated laterally along NE-SW normal faults and strata-bound pathways (i.e., bedding planes), providing hydraulic continuity with permeable structures. The role of pre-existing foliation is further supported by the localization of skarn bodies at the intrusive-marble contact.

Considering all the geological data collected in the area, we can hypothesize that the fluid circulation that enabled the formation of IOCG skarn bodies occurred after the intrusive rocks were formed. Furthermore, assuming the fluid circulation as coeval with the fault activity, it is possible to hypothesize that the skarn formation occurred during the Miocene.

5.2. Mineralogical and Petrographic Considerations and Age Constraints

To estimate the level of the magma emplacement, in four hornblende-bearing samples of dioritic to tonalitic composition, the Al-in-hornblende barometer by [104] was adopted coupled with amphibole-plagioclase thermometry by [105]. Using the rim composition of hornblende and plagioclase (Tables 2 and S1), the simultaneous solution of the two calibrations yielded near-solidus P-T conditions, suitable for estimating the level of magma emplacement. The average pressure was found to be 1.2 $\pm$ 0.2 kbar (at c. 700 °C), corresponding to a crustal depth of 4.4 $\pm$ 0.7 km (Figure 12). Considering the error inherent in the barometer of 0.6 kbar, the uncertainty in the estimate is of c. 2 km.

Concerning the evidence of the α-β quartz transition, witnessed by the polysynthetic twinning of quartz at contact with garnet (Figure 8f), some considerations can be made about the pressure-dependent temperature at which it occurred. Assuming the above estimated pressure value of c. 1.2 kbar, a temperature of the phase transition up to 596 °C can be inferred. This temperature suggests that quartz formed at a high temperature from magmatic-derived fluid as evidenced by fluid inclusion analyses reported in [30], with a progressive cooling process during the late stage of the hydrothermal system characterized by inflow of meteoric water and fluid mixing processes.

Mineralogical and petrographic features observed in the studied skarns align with those reported by [42]. Skarn bodies are characterized by the typical occurrence of both prograde (Grt-dominated and Cpx-dominated assemblages) to retrograde mineralization [30,43] testifying that fluid circulation was prolonged and took place under alternating reducing and oxidant conditions. Retrograde alteration, partially masking the prograde zoning, is characterized by amphibole, epidote and chlorite formation (Cpx-dominated skarn), suggesting later oxidant conditions. Retrograde reducing conditions are evidenced by sulfide precipitation within fractures and cavities in garnet-dominated masses (Figures 7 and 8).

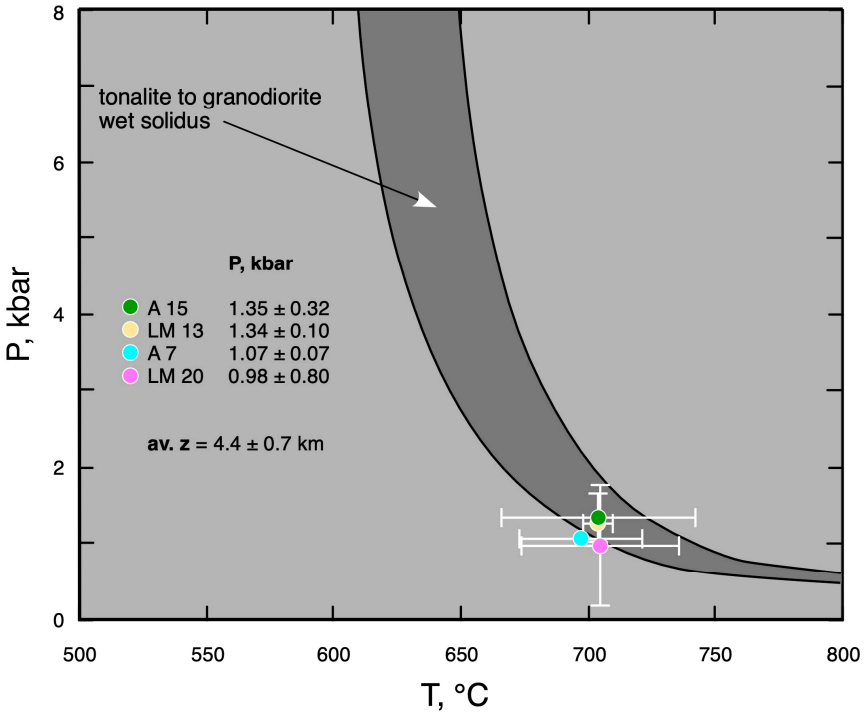

Figure 12. Results of thermobarometry performed on quartz-dioritic to tonalitic samples. P-T values were obtained by combining Al-in-hornblende barometry [104] and amphibole-plagioclase thermometry [105], using the edenite-tremolite thermometer. Tonalite and granodiorite wet solidus are from [106].

Marble, ranging from dolomitic to calcic, reflects the composition of the carbonate protolith, and in the study area is locally affected by intense brittle deformation, which favored late-stage fluid circulation during the retrograde alteration system. Although rare, the skarn also contains olivine, serpentine, and talc, likely related to the more dolomitic composition of the carbonate protolith.

While chalcopyrite and bornite are the main Cu-sulfides occurring in the skarn mined in El Dorado and Juan Bran stocks [42,56], Raman micro-spectroscopy also revealed the occurrence of covellite inclusions through comparison with the literature [70,71]. In particular, this phase was transported by the hydrothermal fluids, which precipitated the host mineral and were trapped within it, and in some vapor-rich inclusions. Covellite is often found as a product of supergene alteration of Cu-bearing mineral. However, hypogene covellite is also found in porphyry copper deposits [107–109], in the deep part of high-sulfidation epithermal deposits [110] and rarely in IOCG system [111,112]. The occurrence of covellite within vapor-rich inclusions provides some information on the fluids carrying this phase. In fact, in the Tatatila-Las Minas IOCG skarn bodies, it is not unusual that both low-salinity vapor-rich fluid inclusions and hypersaline (up to 70 wt.% NaCl) are found in proximity in the same sample, indicating the immiscibility of a magmatic derived fluid at a temperature up to 600 °C [42]. Hypersaline fluid inclusions and fluid immiscibility are typical of the porphyry copper systems and were also reported in IOCG and skarn bodies [69,113,114]. Thus, we infer covellite formed and was transported by the hypersaline fluid, coexisting with a vapor phase, at temperature <507 °C, as covellite is stable below this value [115]. The occurrence of covellite only within quartz and fluid inclusions, suggests that this sulfide precipitated in the fluid under peculiar and local conditions possibly related to the transient decrease of iron concentration in the system which stabilizes this phase (see Figure 8.16 in [115]). However, once the dominant conditions are re-established, the system destabilizes

any covellite that may have precipitated, except those already present within quartz and fluid inclusions.

The $^{40}Ar/^{39}Ar$ analyses performed produced only two significant data, one for a diorite, 15.11 ± 0.40 Ma, and one for a skarn, 13.24 ± 0.14 Ma (LM20 and LM22 in Table 2). Given the shallow intrusion level, the age of the diorite is an acceptable estimate of the age of emplacement. This age is well within the fairly wide age interval, from 16.34 ± 0.20 to 13.92 ± 0.22 Ma, reported by [55], for a suite of intrusive rocks they consider associated with IOCG skarn in the Tatatila-Las Minas bodies. The age of the phlogopite from the skarn, 13.24 ± 0.14 Ma, is instead about 0.7 Ma older than that for the chromian muscovite from retrograde hydrothermal associations reported by [55].

6. Concluding Remarks

The observations and analyses of the IOCG skarn bodies exposed in the Tatatila-Las Minas mining area provide key insights into how mineralization is associated with skarn bodies and why their geometries are challenging to predict. This study highlights that the distribution of Tatatila-Las Minas skarns was primarily controlled by the interplay between structural conduits (e.g., faults and fractures) and pre-existing discontinuities within the rock volumes. These features acted as pathways for high-temperature hydrothermal fluids, whose pressure-driven migration facilitated metasomatism and fluid-rock interaction. The main conclusion is that skarn bodies, formed in geological contexts similar to Tatatila-Las Minas, represent potentially high-volume resources of valuable minerals. Although their subsurface geometries are difficult to predict, we demonstrate that mapping the main structural discontinuities, particularly faults that increase rock mass permeability, can provide predictive criteria for mineral exploration. A structural analysis of faults and fractures constitutes a fundamental first step in exploration protocols and should be complemented by geophysical methods (e.g., magnetotellurics, magnetics, gravimetry) and geochemical investigations. At Tatatila-Las Minas area, we show that skarn bodies locally preserve the geometry of the fault structures that originally facilitated fluid migration, even though subsequent metasomatic overprinting has partially obscured their original fault textures. In sum:

- The distribution of Tatatila–Las Minas IOCG skarns is primarily controlled by structural conduits such as faults and fractures.
- These structures acted as pathways for high-temperature hydrothermal fluids, driving metasomatism and fluid–rock interaction.
- Skarn bodies in similar geological settings represent potentially high-volume mineral resources.
- Although subsurface geometries are challenging to predict, mapping major faults and discontinuities provides key predictive criteria for exploration.
- Skarn bodies locally preserve the geometry of original fault structures, despite partial modification by metasomatic processes.

Supplementary Materials: The following supporting information can be downloaded at: https://www.mdpi.com/article/10.3390/geosciences16010010/s1. Table S1: Summary of the studied samples. Table S2: Selected SEM-EDS analyses of dioritic to tonalitic rocks. Table S3: Analyses (in wt%) of amphiboles (amp), garnets (grt), epidotes (ep), and clinopyroxenes (cpx) performed with WDS (electron microprobe, EMPA) or EDS (scanning electron microscope, SEM). Table S4: $^{40}Ar/^{39}Ar$ analytical table. Isotope intensities (in V) are corrected for blanks, mass discrimination, ^{37}Ar and ^{39}Ar decay, •: data used to calculate ages.

Author Contributions: Conceptualization, M.Z., E.O.-G., D.L. and A.B.; methodology, M.Z., E.O.-G., D.L., A.B., A.C., C.B. and G.R.; software, M.Z., E.O.-G., D.L., A.B. and C.B.; validation, M.Z., E.O.-G.,

D.L., A.B., A.C., M.A.L., W.H.W., C.B., G.M., G.V., A.O. and G.R.; formal analysis, M.Z., E.O.-G., D.L., A.B., A.C., M.A.L., W.H.W., C.B., G.M., G.V., A.O. and G.R.; investigation, M.Z., E.O.-G., D.L., A.B., A.C., W.H.W., C.B., F.G.-A., S.N.-B., A.J.-H. and J.A.G.-A.; resources, D.L. and G.R.; data curation, M.Z., E.O.-G., D.L., A.B., A.C., M.A.L., C.B., G.M., G.V., A.O. and G.R.; writing—original draft preparation, M.Z. and A.B.; writing—review and editing, M.Z., E.O.-G., D.L., A.B., A.C., M.A.L., W.H.W., C.B., F.G.-A., S.N.-B., A.J.-H., J.A.G.-A., G.M., G.V., A.O. and G.R.; supervision, M.Z., D.L., A.B., A.C. and G.R.; funding acquisition, D.L. All authors have read and agreed to the published version of the manuscript.

Funding: This research was supported by European Union's EU Horizon 2020: [Grant Number 727550]; Mexican government: [Grant Number 268074].

Data Availability Statement: The original contributions presented in this study are included in the article. Further inquiries can be directed to the corresponding author.

Acknowledgments: This work is dedicated to the memory of Víctor Hugo Garduño-Monroy, who drove our discussions in the study area and lab but unfortunately and prematurely passed away. We are grateful to four anonymous reviewers, whose constructive comments and suggestions have helped us to improve the original manuscript.

Conflicts of Interest: The authors declare no conflicts of interest.

Appendix A. Samples Preparation and Method

LM13, LM20 and A15 samples were broken into small chips, which were then selected by hand picking, avoiding pieces with noticeable signs of alteration. Selected chips were then hand-crushed and sieved (125–250–350–500 μm fractions). Mineral phases were separated using magnetic methods and a dry shaking table, followed by careful hand-picking under a binocular microscope.

LM22 sample, formed by aggregates of phlogopite, was lightly hand-crushed in an agate mortar, washed, dried, and hand-picked under a microscope.

Amphiboles were leached twice as follows: in CH_3COOH 1M for one hour at room temperature, then thoroughly rinsed in distilled water, and in HNO_3 1N for one hour at 50 °C. Amphiboles and mica were thoroughly rinsed in deionized water and methanol, and dried at about 50 °C on a hot plate.

Samples were wrapped in aluminum foil, packed in a quartz tube together with aliquots of the age monitor TCR sanidine, and irradiated in the core of the 250 kW TRIGA reactor, Pavia University, for five hours.

The samples were then step-heated at the IGG-CNR Ar-Ar laboratory, using the defocused beam of a New Wave Research MIR-10 CO_2 laser as heating device. Ar isotope intensities were measured with a MAP215-50 mass spectrometer operated in peak jumping mode. Raw data were corrected for blanks, mass discrimination, and ^{37}Ar and ^{39}Ar decay. Blanks were run every two to three unknowns, and mass discrimination was monitored through daily analyses of an air pipette. The correction factors for reactor-produced Ar isotopes from Ca and K were mean values obtained from previous longer irradiations on Ca- and K-rich glasses, respectively, in order to have more precise measurements.

The age of the monitor, TCR sanidine, 28.34 Ma, has been recalculated towards an age of 28.198 Ma for FCT sanidine [116] using the intercalibration factor reported by [117].

References

1. Meinert, L.D.; Dipple, G.M.; Nicolescu, S. World Skarn Deposits. In *Economic Geology 100th Anniversary Volume*; Hedenquist, A., Thompson, J.F.H., Goldfarb, R.J., Richards, J.P., Eds.; Society of Economic Geology: Littleton, CO, USA, 2005; Volume 100, pp. 299–336.
2. Sillitoe, R.H. Porphyry Copper Systems. *Econ. Geol.* **2010**, *105*, 3–41. [CrossRef]

3. Einaudi, M.T.; Meinert, L.D.; Newberry, R.J. Skarn Deposits. In *Economic Geology 75th Anniversary Volume*; Skinner, B.J., Ed.; Society of Economic Geology: Littleton, CO, USA, 1981; Volume 75, pp. 317–391.
4. Jowitt, S.M.; Mudd, G.M.; Weng, Z. Hidden mineral deposits in Cu-dominated porphyry-skarn systems: How resource reporting can occlude important mineralization types within mining camps. *Econ. Geol.* **2013**, *108*, 1185–1193. [CrossRef]
5. Sillitoe, R.H. Iron oxide-copper-gold deposits: An Andean view. *Miner. Depos.* **2003**, *38*, 787–812. [CrossRef]
6. Barra, F.; Reich, M.; Selby, D.; Rojas, P.; Simon, A.; Salazar, E.; Palma, G. Unraveling the origin of the Andean IOCG clan: A Re-Os isotope approach. *Ore Geol. Rev.* **2017**, *81*, 62–78. [CrossRef]
7. Ducoux, M.; Branquet, Y.; Jolivet, L.; Arbaret, L.; Grasemann, B.; Rabillard, A.; Gumiaux, C.; Drufin, S. Syn-kinematic skarns and fluid drainage along detachments: The West Cycladic Detachment System on Serifos Island (Cyclades, Greece) and its related mineralization. *Tectonophysics* **2017**, *695*, 1–26. [CrossRef]
8. Vezzoni, S.; Dini, A.; Rocchi, S. Reverse telescoping in a distal skarn system (Campiglia Marittima, Italy). *Ore Geol. Rev.* **2016**, *77*, 176–193. [CrossRef]
9. Tallarico, F.B.H.; Figueiredo, B.R.; Groves, D.I.; Kositcin, N.; McNaughton, N.J.; Fletcher, I.R.; Rego, J.L. Geology and SHRIMP U-Pb Geochronology of the Igarapé Bahia Deposit, Carajás Copper-Gold Belt, Brazil: An Archean (2.57 Ga) Example of Iron-Oxide Cu-Au-(U-REE) Mineralization. *Econ. Geol.* **2005**, *100*, 7–28. [CrossRef]
10. Garduño, V.; Tibaldi, A. Kinematic evolution of the continental active triple junction of the western Mexican Volcanic Belt. *Comptes Rendus L'académie Sci.* **1991**, *312*, 135–142.
11. Pasquarè, G.; Ferrari, L.; Garduño-Monroy, V.H.; Tibaldi, A.; Vezzoli, L. *Geological Map of the Central Sector of the Mexican Volcanic Belt, States of Guanajuato and Michoacan, Mexico*; GSA Maps and Charts Series MCH072; Geological Society of America: Boulder, CO, USA, 1991.
12. Suter, M.; López-Martínez, M.; Quintero-Legorreta, O.; Carrillo-Martínez, M. Quaternary intra-arc extension in the central Trans-Mexican volcanic belt. *Geol. Soc. Am. Bull.* **2001**, *113*, 693–703. [CrossRef]
13. García-Palomo, A.; Macías, J.; Tolson, G.; Valdez, R.; Mora-Chaparro, J. Volcanic stratigraphy and geological evolution of the Apan region, east-central sector of the Transmexican Volcanic Belt. *Geofís. Int.* **2002**, *41*, 133–150. [CrossRef]
14. Gómez-Tuena, A.; Orozco-Esquivel, T.; Ferrari, L. Igneous petrogenesis of the Trans-Mexican Volcanic Belt. In *Geology of México: Celebrating the Centenary of the Geological Society of México; Special Paper*; Alaniz-Álvarez, S.A., Nieto-Samaniego, Á.F., Eds.; Geological Society of America: Boulder, CO, USA, 2007; Volume 422, pp. 1–53.
15. Prol-Ledesma, R.M.; Morán-Zenteno, D.J. Heat Flow and Geothermal Provinces in Mexico. *Geothermics* **2019**, *78*, 183–200. [CrossRef]
16. Olvera-García, E.; Bianco, C.; Garduño-Monroy, V.H.; Brogi, A.; Liotta, D.; Wheeler, W.; Gómez-Alvarez, F.; Najera-Blas, S.; Jiménez-Haro, A.; Guevara-Alday, J.A.; et al. Geology of Las Minas: An example of an exhumed geothermal system (Eastern Trans-Mexican Volcanic Belt). *J. Maps* **2020**, *16*, 918–926. [CrossRef]
17. Ferrari, L.; Orozco-Esquivel, T.; Manea, V.; Manea, M. The dynamic history of the Trans-Mexican Volcanic Belt and the Mexico subduction zone. *Tectonophysics* **2012**, *522–523*, 122–149. [CrossRef]
18. Carrasco-Núñez, G.; López-Martínez, M.; Hernández, J.; Vargas, V. Subsurface stratigraphy and its correlation with the surficial geology at Los Humeros geothermal field, Eastern Trans-Mexican Volcanic Belt. *Geothermics* **2017**, *67*, 1–17. [CrossRef]
19. Carrasco-Nuñez, G.; Bernal, J.P.; Davila, P.; Jicha, B.; Giordano, G.; Hernández, J. Reappraisal of Los Humeros volcanic complex by new U/Th zircon and $^{40}Ar/^{39}Ar$ dating: Implications for greater geothermal potential. *Geochem. Geophys. Geosyst.* **2018**, *19*, 132–149. [CrossRef]
20. Norini, G.; Groppelli, G.; Sulpizio, R.; Carrasco-Núñez, G.; Dávila-Harris, P.; Pellicioli, C.; Zucca, F.; De Franco, R. Structural analysis and thermal remote sensing of the Los Humeros Volcanic Complex: Implications for volcano structure and geothermal exploration. *J. Volcanol. Geoth. Res.* **2015**, *301*, 221–237. [CrossRef]
21. Norini, G.; Carrasco-Núñez, G.; Corbo-Camargo, F.; Lermo, J.; Hernández Rojas, J.; Castro, C.; Bonini, M.; Montanari, D.; Corti, G.; Moratti, G.; et al. The structural architecture of the Los Humeros volcanic complex and geothermal field. *J. Volcanol. Geoth. Res.* **2019**, *381*, 312–329. [CrossRef]
22. Salinas-Rodríguez, J.N.; Lemus-Bustos, O. *Monografía Geológico-Minera del Estado de Veracruz*; Servicio Geológico Mexicano (SGM): Mexico City, Mexico, 2007; 123p.
23. Castro-Mora, J.; Ortíz-Hernández, L.E.; Escamilla-Casas, J.C.; Cruz-Chávez, E.; Dorantes-Castro, C.G. Metalogénesis de la Mineralización Tipo IOCG Relacionada al Skarn del Distrito Minero Las Minas, Estado de Veracruz. *Tópicos Investig. Cienc. Tierra Mater.* **2016**, *3*, 128–143. [CrossRef]
24. Kesler, S.E. Metallogenic evolution of convergent margins: Selected ore deposits models. *Ore Geol. Rev.* **1997**, *12*, 153–171. [CrossRef]
25. Lee, C.-T.A.; Tang, M. How to make porphyry copper deposits. *Earth Planet. Sci. Lett.* **2020**, *529*, 115868. [CrossRef]
26. Hu, X.; Li, H.; Zhu, D.; Bouvier, A.; Wu, J.; Meng, Y. Differentiating Jurassic Cu-, W-, and Sn (–W)-bearing plutons in the Nanling Range (South China): An integrated apatite study. *Ore Geol. Rev.* **2024**, *170*, 106137. [CrossRef]

27. Richards, J.P. Magmatic to hydrothermal metal fluxes in convergent and collided margins. *Ore Geol. Rev.* **2011**, *40*, 1–26. [CrossRef]
28. Deng, C.; Wan, B.; Dong, L.; Talebian, M.; Windley, B.F.; Dadashzadeh, H.; Mohammadi, B.; Barati, B. Miocene porphyry copper deposits in the Eastern Tethyan orogenic belt: Using Sr, O isotopes and Sr/Y ratios to predict the source of ore-related and ore-barren magmas. *Gondwana Res.* **2018**, *62*, 14–26. [CrossRef]
29. Vila, T.; Richard, Z.; Lindsay, N. Geology of the Manto Verde Copper Deposit, Northern Chile: A Specularite-Rich, Hydrothermal-Tectonic Breccia Related to the Atacama Fault Zone. In *Andean Copper Deposits: New Discoveries, Mineralization, Styles and Metallogeny*; Camus, F., Sillitoe, R.M., Petersen, R., Sheahan, P., Eds.; Special Publications of the Society of Economic Geologists: Littleton, CO, USA, 1998; Volume 5, pp. 157–169.
30. Grove, D.I.; Bierlein, F.P.; Meinert, L.D.; Hitzman, M.W. Iron Oxide Copper-Gold (IOCG) Deposits through Earth History: Implications for Origin, Lithospheric Setting, and Distinction from Other Epigenetic Iron Oxide Deposits. *Econ. Geol.* **2010**, *105*, 641–654. [CrossRef]
31. Skirrow, R.G. Iron oxide copper-gold (IOCG) deposits—A review (part 1): Settings, mineralogy, ore geochemistry and classification. *Ore Geol. Rev.* **2022**, *140*, 104569. [CrossRef]
32. Ngo, X.D.; Zhao, X.-F.; Tran, T.H.; Deng, X.-D.; Li, J.-W. Two episodes of REEs mineralization at the Sin Quyen IOCG deposit, NW Vietnam. *Ore Geol. Rev.* **2020**, *125*, 103676. [CrossRef]
33. Corriveau, L.; Mumin, A.H.; Setterfield, T. IOCG environments in Canada: Characteristics, geological vectors to ore and challenges. In *Hydrothermal Iron Oxide Copper-Gold and Related Deposits: A Global Perspective*; Porter, T.M., Ed.; PGC Publishing: Toronto, ON, Canada, 2010; Volume 4, pp. 311–344.
34. Corriveau, L.; Williams, P.J.; Mumin, A.H. Alteration vectors to IOCG mineralization: From uncharted terranes to deposits. In *Exploring for Iron Oxide Copper-Gold Deposits: Canada and Global Analogues*; Corriveau, L., Mumin, A.H., Eds.; Short Course Notes; Geological Association of Canada: St. John's, NL, Canada, 2010; Volume 20, pp. 89–110.
35. Zhao, X.F.; Zhou, M.F. Fe-Cu deposits in the Kangdian region, SW China: A Proterozoic IOCG (iron-oxide-copper-gold) metallogenic province. *Miner. Depos.* **2011**, *46*, 731–747. [CrossRef]
36. Girardi, J.D. Comparison of Mesozoic Magmatic Evolution and Iron Oxide (-Copper-Gold) ('IOCG') Mineralization, Central Andes and Western North America. Master's Thesis, The University of Arizona, Tucson, AZ, USA, 2014.
37. Lopez, G.P.; Hitzman, M.W.; Nelson, E.P. Alteration patterns and structural controls of the El Espino IOCG mining district, Chile. *Miner. Depos.* **2014**, *49*, 235–259. [CrossRef]
38. Skirrow, R.G.; Murr, J.; Schofield, A.; Huston, D.L.; van der Wielen, S.; Czarnota, K.; Coghlan, R.; Highet, L.M.; Doublier, M.; Duan, J. Mapping iron oxide Cu-Au (IOCG) mineral potential in Australia using a knowledge-driven mineral systems-based approach. *Ore Geol. Rev.* **2019**, *113*, 103011. [CrossRef]
39. del Real, I.; Thompson, J.F.H.; Carriedo, J. Lithological and structural controls on the genesis of the candelaria-punta del cobre iron oxide copper gold district, northern Chile. *Ore Geol. Rev.* **2018**, *102*, 106–153. [CrossRef]
40. Bauer, T.E.; Lynch, E.P.; Sarlus, Z.; Drejing-Carroll, D.; Martinsson, O.; Metzger, N.; Wanhainen, C. Structural controls on iron oxide copper-gold mineralisation and related alteration in a Palaeoproterozoic supracrustal belt: Insights from the Nautanen deformation zone and surroundings, Northern Sweden. *Econ. Geol.* **2022**, *117*, 327–359. [CrossRef]
41. del Real, I.; Reich, M.; Simon, A.C.; Deditius, A.; Barra, F.; Rodríguez-Mustafa, M.A.; Thompson, J.F.H.; Roberts, M.P. Formation of giant iron oxide-copper-gold deposits by superimposed episodic hydrothermal pulses. *Sci. Rep.* **2023**, *13*, 12041. [CrossRef] [PubMed]
42. Fuentes-Guzmán, E.; Camprubí, A.; Gonzáles-Partida, E.; Hernández-Avilés, G.; Alfonso, P.; Cienfuegos-Alvarado, E.; Mesino-Hernández, J.C.; Ortega-Obregón, C.; Otero-Trujano, F.J.; Vázquez Ramírez, J.T. The Tatatila–Las Minas IOCG skarn (Veracruz, Mexico): Mineralogical, fluid inclusion and stable isotope constraints. *J. S. Am. Earth Sci.* **2023**, *122*, 104112. [CrossRef]
43. Gómez-Tuena, A.; Mori, L.; Straub, S.M. Geochemical and petrological insights into the tectonic origin of the Transmexican Volcanic Belt. *Earth Sci. Rev.* **2018**, *183*, 153–181. [CrossRef]
44. Demant, A. Caracteristicas del eje neovolcanico transmexicano y sus problemas de interpretación. *Rev. Mex. Cienc. Geol.* **1978**, *2*, 172–187.
45. Ferrari, L.; Orozco-Esquivel, T.; Scott, E.B.; López-Martínez, M.; Silva-Fragoso, A. Cenozoic magmatism and extension in western Mexico: Linking the Sierra Madre Occidental silicic large igneous province and the Comondú Group with the Gulf of California rift. *Earth-Sci. Rev.* **2018**, *183*, 115–152. [CrossRef]
46. Ferrari, L.; Tagami, T.; Eguchi, M.; Orozco-Esquivel, M.; Petrone, C.; Jacobo-Albarrán, J.; López-Martínez, M. Geology, geochronology and tectonic setting of late Cenozoic volcanism along the southwestern Gulf of Mexico: The Eastern Alkaline Province revisited. *J. Volcanol. Geotherm. Res.* **2005**, *146*, 284–306. [CrossRef]
47. Gómez-Tuena, A.; Orozco-Esquivel, T.; Ferrari, L. Petrogénesis ígnea de la Faja Volcánica Transmexicana. *Bol. Soc. Geol. Mex.* **2005**, *57*, 227–285. [CrossRef]

48. García-Palomo, A.; Macías, J.L.; Jiménez, A.; Tolson, G.; Mena, M.; Sánchez-Núñez, J.M.; Arce, J.L.; Layer, P.W.; Santoyo, M.A.; Lermo-Samaniego, J. NW-SE Pliocene- Quaternary extension in the Apan-Acoculco region, eastern Trans-Mexican Volcanic Belt. *J. Volcanol. Geotherm. Res.* **2018**, *349*, 240–255. [CrossRef]
49. Gomez-Alvarez, F.; Garduño-Monroy, V.H.; Sosa-Ceballos, G.; Jiménez-Haro, A.; Liotta, D.; Gaitan-Ramirez, M.F.; Brogi, A.; Israde-Alcántara, I.; Najera-Blas, S.M.; Wheeler, W.; et al. New constraints on tectonism and magmatism from the eastern sector of the Trans-Mexican Volcanic Belt (Chignahuapan Horst, Puebla, México). *J. S. Am. Earth Sci.* **2021**, *112*, 103468. [CrossRef]
50. Israde-Alcántara, I.; Garduño-Monroy, V.H. Lacustrine record in a volcanic intra-arc setting: The evolution of the Late Neogene Cuitzeo basin system (central western Mexico, Michoacán). *Palaeogeogr. Palaeoclimatol. Palaeoecol.* **1999**, *151*, 209–227. [CrossRef]
51. Israde-Alcántara, I.; Domínguez-Vázquez, G.; Gonzalez, S.; Bischoff, J.; West, A.; Huddart, D. Five Younger Dryas black mats in Mexico and their stratigraphic and paleoenvironmental context. *J. Paleolimnol.* **2018**, *59*, 59–79. [CrossRef]
52. Reyes-Guzmán, N.; Siebe, C.; Chevrel, M.O.; Guilbaud, M.N.; Salinas, S.; Layer, P. Geology and radiometric dating of Quaternary monogenetic volcanism in the western Zacapu lacustrine basin (Michoacán, México): Implications for archeology and future hazard evaluations. *Bull. Volcanol.* **2018**, *80*, 18. [CrossRef]
53. Pasquaré, G.; Vezzoli, L.; Zanchi, A. Morphological and structural model of Mexican Volcanic Belt. *Geofís. Int.* **1987**, *26*, 159–176. [CrossRef]
54. Garduño-Monroy, V.H.; Pérez-López, R.; Israde-Alcantara, I.; Rodríguez-Pascua, M.A.; Szynkaruk, E.; Hernández-Madrigal, V.M.; García-Zepeda, M.L.; Corona-Chávez, P.; Ostroumov, M.; Medina-Vega, V.H.; et al. Paleoseismology of the southwestern Morelia–Acambay fault system, central Mexico. *Geofís. Int.* **2009**, *48*, 319–335. [CrossRef]
55. Fuentes-Guzmán, E.; Gonzáles-Partida, E.; Camprubí, A.; Hernández-Avilés, G.; Gabites, J.; Iriondo, A.; Ruggieri, G. The Miocene Tatatila–Las Minas IOCG skarn deposits (Veracruz) as a result of adakitic magmatism in the Trans-Mexican Volcanic Belt. *Bol. Soc. Geol. Mex. Sci.* **2020**, *72*, A110520. [CrossRef]
56. Mexican Gold Mining, Preliminary Economic Assessment 2021 and Technical Report. Available online: https://mexicangold.ca/las-minas/ (accessed on 1 October 2024).
57. Laurenzi, M.A.; Branchi, E.; Casalini, M.; Conticelli, S. New ^{40}Ar-^{39}Ar dating and revision of the geochronology of the Monte Amiata Volcano, Central Italy. *Ital. J. Geosci.* **2015**, *134*, 255–265. [CrossRef]
58. Koppers, A.A.P. ArArCALC—Software for ^{40}Ar/^{39}Ar age calculations. *Comput. Geosci.* **2002**, *28*, 605–619. [CrossRef]
59. Ludwig, K.R. *Isoplot 3.75—A Geochronological Toolkit for Microsoft Excel*; Special Publication 5; Berkeley Geochronology Center: Berkeley, CA, USA, 2012.
60. Steiger, R.H.; Jäger, E. Subcommission on geochronology: Convention on the use of decay constants in geo- and cosmochronology. *Earth Planet. Sci. Lett.* **1977**, *36*, 359–362. [CrossRef]
61. Min, K.; Mundil, R.; Renne, P.R.; Ludwig, K.R. A test for systematic errors in ^{40}Ar/^{39}Ar geochronology through comparison with U–Pb analysis of a 1.1 Ga rhyolite. *Geochim. Cosmochim. Acta* **2000**, *64*, 73–98. [CrossRef]
62. Whitney, D.L.; Evans, B.W. Abbreviations for names of rock-forming minerals. *Am. Mineral.* **2010**, *95*, 185–187. [CrossRef]
63. Cawthorn, T.G.; Brown, M.P. A model for the formation and crystallization of corundum normative calc-alkaline magmas through amphibole fractionation. *J. Geol.* **1976**, *84*, 467–476. [CrossRef]
64. Boynton, W.V. Geochemistry of the rare earth elements: Meteorite studies. In *Rare Earth Element Geochemistry*; Henderson, P., Ed.; Elsevier: Amsterdam, The Netherlands, 1984; pp. 63–114.
65. Bachheimer, J.P. An anomaly in the β phase near the α-β transition of quartz. *J. Phys. Lett.* **1980**, *41*, L-559–L-561. [CrossRef]
66. Dolino, G.; Bachheimer, J.P.; Zeyen, C.M.E. Observation of an intermediate phase near the α-β transition of quartz by heat capacity and neutron scattering measurements. *Solid State Commun.* **1983**, *45*, 295–299. [CrossRef]
67. Spearing, D.R.; Farnan, I.; Stebbins, J.F. Dynamics of the α-β phase transitions in quartz and cristobalite as observed by in-situ high temperature ^{29}Si and ^{17}O NMR. *Phys. Chem. Miner.* **1992**, *19*, 307–321. [CrossRef]
68. Tuttle, O.F. Structural petrology of planes of liquid inclusions. *J. Geol.* **1949**, *57*, 331–356. [CrossRef]
69. Roedder, E. Fluid inclusions. *Rev. Mineral.* **1984**, *12*, 644.
70. Ishii, M.; Shibata, K.; Nozaki, H. Anion Distributions Phase Transitions in CuS1-xSe x(x = 0–1) Studied by Raman Spectroscopy. *J. Solid State Chem.* **1993**, *105*, 504–511. [CrossRef]
71. Hurma, T.; Kose, S. XRD Raman analysis and optical properties of CuS nanostructured film. *Optik* **2016**, *127*, 6000–6006. [CrossRef]
72. Vidale, R.J. Metasomatism in chemical gradient and formation of calc-silicate bands. *Am. J. Sci.* **1969**, *267*, 857–874. [CrossRef]
73. Kerrick, D.M. The genesis of zoned skarns in the Sierra Nevada, California. *J. Petrol.* **1977**, *18*, 144–181. [CrossRef]
74. Meinert, L.D. Skarn and skarn deposits. *Geosci. Can.* **1992**, *19*, 145–162.
75. Harlov, D.E.; Austrheim, H. *Metasomatism and the Chemical Transformation of Rock—The Role of Fluids in Terrestrial and Extraterrestrial Processes*; Lecture Notes in Earth System Sciences; Springer: Berlin/Heidelberg, Germany, 2013; pp. 1–16.
76. Hantsche, A.L.; Kouzmanov, K.; Milenkov, G.; Vezzoni, S.; Vassileva, R.; Dini, A.; Sheldrake, T.; Laurent, O.; Guillong, M. Metasomatism and cyclic skarn growth along lithological contacts: Physical geochemical evidence from a distal Pb-Zn skarn. *Lithos* **2021**, 400–401, 106408. [CrossRef]

77. Tinagli, L.; Paoli, G.; Vezzoni, S. Snake-shaped carbonate folds replaced by skarn (Campiglia Marittima, Italy). *Int. J. Earth Sci.* **2021**, *110*, 113–114. [CrossRef]
78. Vezzoni, S.; Rocchi, S.; Dini, A. Campiglia Marittima Skarn (Tuscany): A Challenging Example for the Evolution of Skarn-Forming Models. *Minerals* **2023**, *13*, 482. [CrossRef]
79. Zucchi, M.; Tursi, F.; Brogi, A.; Liotta, D.; Spiess, R.; Caggianelli, A.; Ventruti, G.; Langone, A. Syn-tectonic contact aureole and metasomatic reaction zones in carbonate and pelitic host rocks (Elba Island, Italy). *Tectonophysics* **2023**, *853*, 229782. [CrossRef]
80. Meinert, L.D. Application of skarn deposit zonation models to mineral exploration. *Explor. Min. Geol.* **1997**, *6*, 185–208.
81. Chang, Z.; Meinert, L.D. Zonation in skarn—Complexities and controlling factors. In Proceedings of the PacRim Congress 2008, Gold Coast, QLD, Australia, 24–26 November 2008; Volume 11, pp. 303–306.
82. Malehmir, A.; Dahlin, P.; Lundberg, E.; Juhlin, C.; Sjöström, H.; Högdahl, K. Reflection seismic investigations in the Dannemora area, central Sweden: Insights into the geometry of polyphase deformation zones and magnetite-skarn deposits. *J. Geophys. Res.* **2011**, *116*, B11307. [CrossRef]
83. Curewitz, D.; Karson, J.A. Structural settings of hydrothermal outflow: Fracture permeability maintained by fault propagation and interaction. *J. Volcanol. Geotherm. Res.* **1997**, *79*, 149–168. [CrossRef]
84. Caine, J.S.; Evans, J.P.; Forster, C.B. Fault zone architecture and permeability structure. *Geology* **1996**, *24*, 1025–1028. [CrossRef]
85. Sibson, R.H. Fluid involvement in normal faulting. *J. Geodyn.* **2000**, *29*, 469–499. [CrossRef]
86. Cox, S.F.; Knackstedt, M.A.; Braun, J. *Principles of Structural Control on Permeability and Fluid Flow in Hydrothermal Systems (Structural Controls on Ore Genesis)*; Society of Economic Geologists: Littleton, CO, USA, 2001; Chapter 24; pp. 1–24.
87. Sillitoe, R.H.; Brogi, A. Geothermal systems in the northern Apennines, Italy: Modern analogues of Carlin-style gold deposits. *Econ. Geol.* **2021**, *116*, 1491–1501. [CrossRef]
88. Faulds, J.E.; Coolbaugh, M.F.; Vice, G.S.; Edwards, M.L. Characterizing Structural Controls of Geothermal Fields in the Northwestern Great Basin: A Progress Report. *Geotherm. Resour. Counc. Trans.* **2006**, *30*, 69–76.
89. Cashman, P.H.; Faulds, J.E.; Hinz, N.H. Regional Variations in Structural Controls on Geothermal Systems in the Great Basin. *GRC Trans.* **2012**, *36*, 25–30.
90. Nukman, M.; Moeck, I. Structural controls on a geothermal system in the Tarutung Basin, north central Sumatra. *J. Asian Earth Sci.* **2013**, *74*, 86–96. [CrossRef]
91. Arzate, J.; Corbo-Camargo, F.; Carrasco-Núñez, G.; Hernández, J.; Yutsis, V. The Los Humeros (Mexico) geothermal field model deduced from new geophysical and geological data. *Geothermics* **2018**, *71*, 200–211. [CrossRef]
92. Liotta, D.; Brogi, A. Pliocene-Quaternary fault kinematics in the Larderello geo-thermal area (Italy): Insights for the interpretation of the present stress field. *Geothermics* **2020**, *83*, 101714. [CrossRef]
93. Olvera-García, E.; Garduño-Monroy, V.H.; Liotta, D.; Brogi, A.; Bermejo-Santoyo, G.; Guevara-Alday, A. Neogene-Quaternary normal and transfer faults controlling deep-seated geothermal systems: The case of San Agustín del Maíz (central Trans-Mexican Volcanic Belt, México). *Geothermics* **2020**, *86*, 101791. [CrossRef]
94. Taussi, M.; Brogi, A.; Liotta, D.; Nisi, B.; Perrini, M.; Vaselli, O.; Zambrano, M.; Zucchi, M. CO_2 and heat energy transport by enhanced fracture permeability in the Monterotondo Marittimo-Sasso Pisano transfer fault system (Larderello Geothermal Field, Italy). *Geothermics* **2022**, *105*, 102531. [CrossRef]
95. Person, M.; Banerjee, A.; Hofstra, A.; Sweetkind, D.; Gao, Y. Hydrologic models of modern and fossil geothermal systems in the Great Basin: Genetic implications for epithermal Au-Ag and Carlin-type gold deposits. *Geosphere* **2008**, *4*, 888–917. [CrossRef]
96. Liotta, D.; Brogi, A.; Ruggieri, G.; Rimondi, V.; Zucchi, M.; Helgadóttir, H.M.; Montegrossi, G.; Friðleifsson, G.Ó. Fracture analysis hydrothermal mineralization fluid pathways in the Neogene Geitafell central volcano: Insights for the Krafla active geothermal system Iceland. *J. Volcanol. Geoth. Res.* **2020**, *391*, 106502. [CrossRef]
97. Brogi, A.; Alçiçek, M.C.; Liotta, D.; Capezzuoli, E.; Zucchi, M.; Matera, P.F. Step-over fault zones controlling geothermal fluid-flow and travertine formation (Denizli Basin, Turkey). *Geothermics* **2021**, *89*, 101941. [CrossRef]
98. Zucchi, M.; Brogi, A.; Liotta, D.; Caggianelli, A.; Dini, A.; Ventruti, G.; Ruggieri, G.; Matera, P.F. Fractures, fluid flow and inherited structures in geothermal systems: Inputs from the Fe-ore deposits of eastern Elba Island (Northern Apennines, Italy). *Geol. Mag.* **2022**, *159*, 2238–2261. [CrossRef]
99. Sosa-Ceballos, G.; Macías, J.L.; Avellán, D.R.; Salazar-Hermenegildo, N.; Boijseauneau-López, M.E.; Pérez- Orozco, J.D. The Acoculco Caldera Complex magmas: Genesis, evolution and relation with the Acoculco geothermal system. *J. Volcanol. Geoth. Res.* **2018**, *358*, 288–306. [CrossRef]
100. Avellán, D.R.; Macías, J.L.; Layer, P.W.; Sosa-Ceballos, G.; Gómez-Vasconcelos, M.G.; Cisneros-Máximo, G.; Sánchez-Núñez, J.M.; Martí, J.; García-Tenorio, F.; López-Loera, A.P.; et al. Eruptive chronology of the Acoculco caldera complex—A resurgent caldera in the eastern Trans-Mexican Volcanic Belt (México). *J. S. Am. Earth Sci.* **2020**, *98*, 102412. [CrossRef]
101. Alçiçek, M.C.; Brogi, A.; Capezzuoli, E.; Liotta, D.; Meccheri, M. Superimposed basins formation during the Neogene–Quaternary extensional tectonics in SW-Anatolia (Turkey): Insights from the kinematics of the Dinar Fault Zone. *Tectonophysics* **2013**, *608*, 713–727. [CrossRef]

102. Brogi, A.; Israde, I.; Sigurveig, A.; Capezzuoli, E. Tectonic control on travertine and silica sinter deposition in oceanic transform-fault setting: The case of the Lýsuskarð volcano-geothermal area, Snæfellsnes Peninsula, Iceland. *Int. Geol. Rev.* **2023**, *65*, 3287–3310. [CrossRef]
103. Sanderson, D.J.; Nixon, C.W. Topology, connectivity and percolation in fracture networks. *J. Struct. Geol.* **2018**, *115*, 167–177. [CrossRef]
104. Anderson, J.L.; Smith, D.R. The effects of temperature and fo_2, on the Al-in-hornblende barometer. *Am. Min.* **1995**, *80*, 549–559. [CrossRef]
105. Holland, T.; Blundy, J. Non-ideal interactions in calcic amphiboles and their bearing on amphibole-plagioclase thermometry. *Contrib. Mineral. Petrol.* **1994**, *116*, 433–447. [CrossRef]
106. Schmidt, M.W.; Thompson, A.B. Epidote in calc-alkaline magmas: An experimental study of stability, phase relationships, and the role of epidote in magmatic evolution. *Am. Min.* **1996**, *81*, 462–474. [CrossRef]
107. Ossandón, C.G.; Fréraut, C.R.; Gustafson, L.B.; Lindsay, D.D.; Zentilli, M. Geology of the Chuquicamata Mine: A Progress Report. *Econ. Geol.* **2001**, *96*, 249–270. [CrossRef]
108. Khashgerel, B.-E.; Rye, R.O.; Hedenquist, J.W.; Kavalieris, I. Geology and reconnaissance, stable isotope study of the Oyu Tolgoi porphyry Cu-Au system, South Gobi, Mongolia. *Econ. Geol.* **2006**, *101*, 503–522. [CrossRef]
109. Yousefi Soorani, L.; Shafiei Bafti, B.; Homam, S.M.; Abbasloo, Z.; Taghizadeh Zanooghi, H. Hypogene enrichment in Miduk porphyry copper ore deposit, Iran. *Sci. Rep.* **2022**, *12*, 19133. [CrossRef] [PubMed]
110. Hedenquist, J.W.; Arribas, A., Jr.; Gonzalez-Urien, E. Exploration for epithermal gold deposits. *Rev. Econ. Geol.* **2000**, *13*, 245–277.
111. Cave, B.; Lilly, R.; Hand, M.; Varga, J.; Light, S.; Leslie, D.; North, B.; Park, J.; Klingberg, L. A temporal framework for the Carrapateena Iron Oxide Copper-Gold (IOCG) deposit, Eastern Gawler Craton, South Australia. *Ore Geol. Rev.* **2024**, *169*, 106092. [CrossRef]
112. Sorrentino, A.; Chirico, R.; Corrado, F.; Laukamp, C.; Martire, D.D.; Mondillo, N. The application of PRISMA hyperspectral satellite imagery in the delineation of distinct hydrothermal alteration zones in the Chilean Andes: The Marimaca IOCG and the Río Blanco-Los Bronces Cu-Mo porphyry districts. *Ore Geol. Rev.* **2024**, *167*, 105998. [CrossRef]
113. Bodnar, R.J.; Lecumberri-Sanchez, P.; Moncada, D.; Steele-MacInnis, M. Fluid Inclusions in Hydrothermal Ore Deposits. In *Treatise on Geochemistry*, 2nd ed.; Holland, H.D., Turekian, K.K., Eds.; Elsevier: Oxford, UK, 2014; Volume 13, pp. 119–142.
114. Baker, T.; Mustard, R.; Fu, B.; Williams, P.J.; Dong, G.; Fisher, L.; Mark, G.; Ryan, C.G. Mixed messages in iron-oxide-copper-gold systems of the Cloncurry district, Australia: Insights from PIXE analysis of halogens and copper in fluid inclusions. *Miner. Depos.* **2008**, *43*, 599–608. [CrossRef]
115. Vaughan, D.J.; Craig, J.R. Sulfide ore stabilities, morphologies and intergrowth textures. In *Geochemistry of Hydrothermal Ore Deposits*, 3rd ed.; Barnes, H.L., Ed.; Wiley: New York, NY, USA, 1997; pp. 367–434.
116. Kuiper, K.F.; Deino, A.; Hilgen, F.J.; Krijgsman, W.; Renne, P.R.; Wijbrans, J.R. Synchronizing rock clocks of Earth history. *Science* **2008**, *320*, 500–504. [CrossRef]
117. Renne, P.R.; Swisher, C.C.; Deino, A.L.; Karner, D.B.; Owens, T.L.; Depaolo, D.J. Inter-calibration of standards, absolute ages and uncertainties in $^{40}Ar/^{39}Ar$ dating. *Chem. Geol.* **1998**, *145*, 117–152. [CrossRef]

Disclaimer/Publisher's Note: The statements, opinions and data contained in all publications are solely those of the individual author(s) and contributor(s) and not of MDPI and/or the editor(s). MDPI and/or the editor(s) disclaim responsibility for any injury to people or property resulting from any ideas, methods, instructions or products referred to in the content.